

Jet-installation noise and near-field characteristics of jet–surface interaction

*Original*

Jet-installation noise and near-field characteristics of jet–surface interaction / Rego, L.; Avallone, F.; Ragni, D.; Casalino, D.. - In: JOURNAL OF FLUID MECHANICS. - ISSN 1469-7645. - 895:(2020), p. A2. [10.1017/jfm.2020.294]

*Availability:*

This version is available at: 11583/2976927 since: 2023-03-14T10:49:34Z

*Publisher:*

Cambridge University Press

*Published*

DOI:10.1017/jfm.2020.294

*Terms of use:*

This article is made available under terms and conditions as specified in the corresponding bibliographic description in the repository

*Publisher copyright*

(Article begins on next page)

# Jet-installation noise and near-field characteristics of jet–surface interaction

L. Rego<sup>1,†</sup>, F. Avallone<sup>1</sup>, D. Ragni<sup>1</sup> and D. Casalino<sup>1</sup>

<sup>1</sup>Delft University of Technology, Department of Aerodynamics, Wind Energy and Propulsion, Kluyverweg 1, 2629 HS Delft, The Netherlands

(Received 25 November 2019; revised 30 March 2020; accepted 8 April 2020)

The link between jet-installation noise and the near-field flow features of the corresponding isolated jet is studied by means of lattice-Boltzmann numerical simulations. The computational set-up consists of a flat plate placed in proximity to a jet, replicating the interaction benchmark study carried out at NASA Glenn. Installation effects cause low-frequency noise increase with respect to the isolated case, mainly occurring in the direction normal to the plate and upstream of the jet's exit plane. It is shown that the Helmholtz number, based on the wavelength of eddies in the mixing layer and their distance to the plate trailing edge, predicts the frequency range where installation noise occurs. Based on the isolated jet near field, scaling laws are also found for the far-field noise produced by different plate geometries. The linear hydrodynamic field of the isolated jet shows an exponential decay of pressure fluctuations in the radial direction; it is shown that the far-field spectrum follows the same trend when moving the plate in this direction. In the axial direction, spectral proper orthogonal decomposition is applied to filter out jet acoustic waves. The resultant hydrodynamic pressure fluctuations display a wavepacket behaviour, which can be fitted with a Gaussian envelope. It is found that installation noise for different plate lengths is proportional to the amplitude of the Gaussian curve at the position of the plate trailing edge. These analyses show that trends of jet-installation noise can be predicted by analysing the near field of the isolated case, reducing the need for extensive parametric investigations.

**Key words:** aeroacoustics, jet noise

## 1. Introduction

High-bypass-ratio turbofans have the potential to reduce environmental and acoustic emissions with respect to conventional jet engines, mainly due to a relatively lower exhaust flow velocity  $U_j$ , which increases their overall efficiency (Huff 2007). As a consequence, jet noise resulting from turbulent flow mixing is decreased due to the strong dependence of the acoustic intensity on the jet flow speed ( $I \propto U_j^8$ )

<sup>†</sup> Email address for correspondence: [l.rego@tudelft.nl](mailto:l.rego@tudelft.nl)

(Lighthill 1952). The progressive increase of bypass ratio results in a closer coupling between engine and lifting surfaces; as engines become larger, their distance from the wing needs to be reduced in order to ensure minimum ground clearance. Thus, the interaction between the hydrodynamic near field of the jet and the nearby lifting surface results in an additional noise source at the trailing edge of the latter, thus causing noise amplification at low and mid-frequencies (jet-installation effects) (Mengle *et al.* 2006; Belyaev *et al.* 2015). Jet-installation noise (JIN) is stronger during take-off and approach since high-lift devices are typically deployed and positioned closer to the jet plume (Brown & Ahuja 1984). Recent computational results of aircraft acoustic footprint have shown that installation effects are responsible for penalties of approximately 4 EPNdB (effective perceived noise in decibels) at full aircraft level (Casalino & Hazir 2014). These noise sources and penalties are especially relevant during approach and landing, for which the jet noise contribution is typically neglected in preliminary aeroacoustic assessments (Casalino & Hazir 2014).

Jet-installation noise is typically investigated by placing a solid surface near a jet and varying the location and/or length of the surface trailing edge with respect to the jet axis and nozzle exit plane (Lawrence, Azarpeyvand & Self 2011; Cavalieri *et al.* 2014). When the surface is placed in the jet acoustic field, where hydrodynamic convective terms can be neglected, the diffraction of acoustic waves from quadrupole sources is predominant; consequently, no significant change of the overall far-field noise intensity relative to the isolated case is found (Cavalieri *et al.* 2014). Instead, if the surface is located in the irrotational region of the jet hydrodynamic field, a strong sound amplification is caused by the scattering of convecting pressure waves at the trailing edge of the solid surface (Cavalieri *et al.* 2014; Lyu, Dowling & Naqavi 2017). Ffowcs-Williams & Hall (1970) showed that this is caused by a change of impedance seen by those hydrodynamic pressure waves at the geometric discontinuity (i.e. the trailing edge). The sound intensity of this source scales with the fifth power of the jet velocity ( $I \propto U_j^5$ ), thus becoming relevant at subsonic Mach numbers (Ffowcs-Williams & Hall 1970). Finally, if the surface is placed inside the rotational region of the jet, there is an additional component of turbulent boundary-layer trailing-edge noise due to grazing flow (Brown 2012; Piantanida *et al.* 2016). For aircraft, JIN typically refers to the second type of interaction (i.e. surface immersed in the irrotational field), since direct grazing is usually prevented due to the high velocity and temperature of the jet.

The effect of the solid surface is not only to increase noise intensity, but also to change the acoustic directivity and the far-field spectral characteristics. Isolated jets typically feature a broadband spectrum with a super-directive behaviour, i.e. noise increases exponentially when approaching polar angles in the downstream direction of the jet axis (Cavalieri *et al.* 2012). On the other hand, spectra for installed jets are characterized by sound amplification in the low and mid-frequency range due to trailing-edge scattering, whereas at higher frequencies, the surface causes reflection or shielding of acoustic waves generated by quadrupole sources (Head & Fisher 1976). The sound directivity is consistent with the presence of additional dipole sources at the trailing edge: in the azimuthal direction, there are two lobes in the direction normal to the surface, while no noise increase is found in the direction of the surface plane; in the polar direction, a cardioid pattern is present, with maximum amplification in the upstream direction of the jet; in the downstream direction along the jet axis, noise levels are similar to those of the isolated configuration (Head & Fisher 1976).

When there is no significant deformation of the jet flow field caused by the solid surface, JIN can be linked to the near-field properties of the corresponding isolated

jet, as if no surface is present (Ffowcs-Williams & Hall 1970; Cavalieri *et al.* 2014). Therefore, this work aims at developing methodologies that allow for the prediction of the frequency range and the relative noise increase when changing the solid surface location and length, using information of the jet near field.

Ffowcs-Williams & Hall (1970) and Crighton & Leppington (1970) related JIN to the wavelength of eddies in the near-hydrodynamic field with respect to their location from the trailing edge. This relationship is described through inequalities that predict whether the hydrodynamic field generated by those structures is responsible for noise amplification, when scattered by the surface. The effect of source compactness on edge scattering was also studied by Cavalieri *et al.* (2014) and Roger, Moreau & Kucukcoskun (2016). The latter showed that the cardioid directivity pattern is characteristic of sources with relatively low Helmholtz number, i.e. wavelength non-compact with respect to the trailing-edge distance. Moreover, structures with lower Helmholtz number produce more noise when scattered at the edge (Roger *et al.* 2016). The source position, however, is not arbitrary; it must be located within the turbulent flow, and it is dependent on the characteristics of the mixing layer. This work shows that, with an equivalent source location and the compactness inequalities described by Ffowcs-Williams & Hall (1970), it is possible to predict the frequency range where the edge scattering is the dominant noise mechanism. Therefore, a methodology such as the one proposed in this work, which can properly locate equivalent sources in a jet, can provide realistic trends for installation effects.

For the amplitude of the installed jet spectra, Cavalieri *et al.* (2014) reported an exponential increase in noise levels as the plate is moved towards the jet, in agreement with the characteristics of the irrotational hydrodynamic field. A similar analysis for the axial direction might be used to link the convection and development of the pressure waves from the jet to the installed far-field noise for different surface lengths.

Papamoschou (2010), using an analytical approach, concluded that noise from trailing-edge scattering is correlated to the wavepacket features of the jet. Therefore, in order to properly characterize the hydrodynamic near field, the development of coherent turbulent structures in the mixing layer must be investigated (Arndt, Long & Glauser 1997; Suzuki & Colonius 2006; Tinney & Jordan 2008). The spectral proper orthogonal decomposition (SPOD) technique is applied for this purpose. The SPOD decomposes an unsteady flow time series into a sequence of frequency-dependent modes (Schmidt *et al.* 2018; Towne, Schmidt & Colonius 2018). When applied to a pressure time series from the jet flow, the resulting streamwise eigenfunctions show a characteristic growth, saturation and decay of pressure fluctuations, which agrees with the behaviour of instability waves or wavepackets (Papamoschou 2010; Cavalieri *et al.* 2012). This strategy was also adopted by Suzuki & Colonius (2006), who analysed the results from eigenvectors of cross-spectral matrices obtained from near-field pressure measurements. The results showed a good agreement with those from linear stability theory, with the instability-wave envelope captured for a wide range of frequencies.

In this work, the characteristics of the jet hydrodynamic pressure fluctuations are investigated in both radial and axial directions, and the trends are used as scaling parameters for the spectra obtained for different flat-plate positions and lengths. Through the scaling laws found in this paper, the acoustic characteristics of JIN can be predicted using its isolated jet analogue, reducing the computational and experimental costs associated with the analysis of several geometries.

The study is carried out with a lattice-Boltzmann solver coupled with a very-large-eddy simulation model (LBM-VLES). This method has been chosen since it can

resolve the flow field with a relatively low computational cost, but still show very good agreement with experimental data, as shown by van der Velden *et al.* (2018) for an isolated jet. The installed jet configuration investigated in this paper replicates the one from the jet–surface interaction benchmark study performed at NASA Glenn, with a single-stream nozzle and a nearby flat plate (Brown 2012; Podboy 2013). The experimental results from this benchmark study are used for validation of the installed jet set-up.

This paper is organized as follows. In § 2, the high-fidelity flow simulation model is discussed, with a brief description of the LBM-VLES. In § 3, the studied cases and their computational set-ups are described. In § 4, the mesh convergence study is shown and the computational results are validated against experimental data (Brown & Bridges 2006; Brown 2012). The far-field noise results are reported in § 5, along with a near-field analysis of the trailing-edge scattering for the installed case. The effect of source compactness on the far-field noise is assessed in § 6. The effect of the plate radial and axial positions relative to the jet is addressed in § 7, with the development of scaling laws for the far-field spectra. Finally, the most important findings of this work are summarized in the conclusions in § 8.

## 2. Flow simulation model

The lattice-Boltzmann method (LBM) solves the discrete form of the Boltzmann equation by using particle distribution functions to simulate the macroscopic flow properties. Through local integration of these particle distribution functions, the flow density, momentum and internal energy are obtained (Succi 2001). The solution of the Boltzmann equation is performed on a Cartesian mesh (lattice), with an explicit time integration and collision model:

$$f_i(\mathbf{x} + \mathbf{c}_i \Delta t, t + \Delta t) - f_i(\mathbf{x}, t) = C_i(\mathbf{x}, t), \quad (2.1)$$

with  $f_i$  representing the particle distribution function along the  $i$ th lattice direction. The particle motion is statistically described at a position  $\mathbf{x}$  with a discrete velocity  $\mathbf{c}_i$  in the  $i$ -direction at the time  $t$ . The space and time increments are represented by  $\mathbf{c}_i \Delta t$  and  $\Delta t$ , respectively. For the collision term  $C_i(\mathbf{x}, t)$ , the employed formulation is based on a Galilean invariant for thermal flows of non-unitary Prandtl number (Chen, Gopalakrishnan & Zhang 2014). The equilibrium Maxwell–Boltzmann distribution  $f_i^{eq}$  is adopted (Chen, Chen & Matthaeus 1992). The distribution functions are projected on a basis of Hermite polynomials and the moments are computed over a discrete set of particle velocities, using Gaussian quadrature formulae for different lattices (Chen *et al.* 2014). For this work, a 19-state lattice, known as D3Q19, is adopted.

Given the high Reynolds number of the jet flow, a very-large-eddy simulation (VLES) model accounts for the unresolved scales of turbulence. A modified two-equation  $k$ – $\epsilon$  renormalization group (RNG) turbulence model is employed to compute a turbulent relaxation time that is added to the viscous relaxation time (Yakhot & Orszag 1986):

$$\tau_{eff} = \tau + C_\mu \frac{k^2/\epsilon}{(1 + \eta^2)^{1/2}}, \quad (2.2)$$

where  $C_\mu = 0.09$ , and  $\eta$  is a combination of the local strain, local vorticity and local helicity parameters (Yakhot *et al.* 1992). The term  $\eta$  allows for the mitigation of the subgrid-scale viscosity, so that the resolved large-scale structures are not numerically

damped. The relaxation time is then used to adapt the Boltzmann model to the characteristic time scales of a turbulent flow motion. Hence, the Reynolds stresses are not explicitly added to the governing equations, but they are an implicit consequence of the chaotic exchange of momentum driven by the turbulent flow, with characteristic times smaller than the slowly varying turbulent flow. The Reynolds stresses then have a nonlinear structure and are better suited to represent turbulence in a state far from equilibrium, as in the presence of distortion, shear and rotation (Chen *et al.* 2004). A wall model is also adopted to approximate the no-slip boundary conditions, which is based on an extension of the generalized law-of-the-wall model, taking into account the effect of pressure gradients (Launder & Spalding 1974).

The low dissipation and dispersion of the LBM, coupled with a compressible and time-dependent solution, allow the sound field to be extracted directly from the pressure field (Brès, Pérot & Freed 2009). However, this approach would require a fairly large computational domain with respect to the nozzle and plate dimensions. A high degree of mesh refinement would also be necessary, even at regions far from the jet/surface, so that the number of points per wavelength would be sufficient for high-frequency far-field analyses. Therefore, to avoid high computational costs, the far-field noise is computed through the Ffowcs-Williams and Hawkings analogy (Ffowcs-Williams & Hawkings 1969), adopting the formulation 1A from Farassat & Succi (1980), extended to a convective wave equation (Brès, Pérot & Freed 2010). The formulation is implemented in the time domain using a source-time-dominant algorithm (Casalino 2003).

A permeable surface is defined to include all the relevant noise sources, i.e. dipoles on the plate trailing edge and quadrupoles in the jet (da Silva *et al.* 2015). Pressure and velocity fluctuations recorded on this surface are used for far-field noise estimation. A more detailed description of the FWH surface is reported in §3.2. In addition, the FWH analogy can be applied to the pressure fluctuations on the solid plate surface, in order to isolate the noise contribution from the acoustic dipoles.

The methodology described above is implemented in the commercial software Simulia PowerFLOW 6-2019. This software has also been used and validated for aero-engine aeroacoustic applications to predict fan broadband noise in subsonic (Casalino, Hazir & Mann 2017; Casalino *et al.* 2019) and transonic (Gonzalez-Martino & Casalino 2018) conditions. A validation study for the isolated SMC000 jet has been accomplished by van der Velden *et al.* (2018), showing a very good agreement with experimental results. For an installed jet, computations were performed by da Silva *et al.* (2015). The results, in terms of far-field noise spectra, also showed a good agreement with experimental data, indicating the capability of the solver to accurately predict JIN.

### 3. Numerical set-up

#### 3.1. Installed jet configurations and flow conditions

The installed jet model replicates the NASA Glenn benchmark experiments (Brown 2012; Podboy 2013), where a flat plate is placed in the vicinity of a single-stream jet nozzle (SMC000). The SMC000 is a round, convergent nozzle with an exit diameter  $D_j = 50.8$  mm, used for studies on subsonic jets (Brown & Bridges 2006). The primary convergent nozzle has a 152 mm diameter inlet, followed by a contraction with a 5° taper angle up to the exit plane.

Different geometric configurations are investigated, for which the length and height of the plate are varied. As shown in figure 1, the length  $L$  is defined as the distance

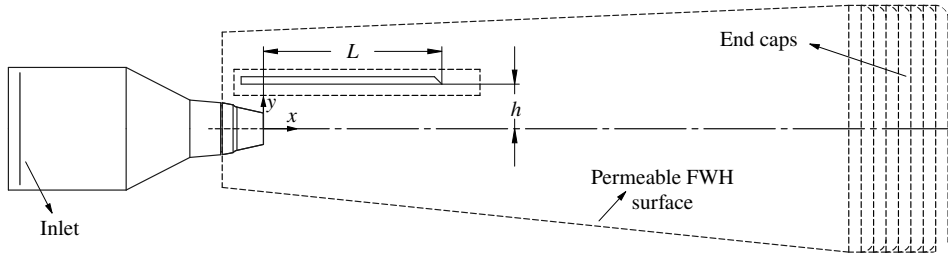


FIGURE 1. Schematic of the computational set-up, with the flat-plate length  $L$  and height  $h$ . A permeable FWH surface encompasses the jet and the flat plate. Caps are placed at the downstream end of the surface, and cutouts are placed in the regions of the plate and nozzle.

	$h = 1.0D_j$	$h = 1.25D_j$	$h = 1.5D_j$
$L = 4D_j$	X	X	X
$L = 5D_j$	—	X	X
$L = 6D_j$	—	X	X

TABLE 1. Investigated geometric cases, based on the flat-plate length  $L$  and height  $h$ .

Setpoint	NPR	$T_R$	$M_a$	$Re$
01	1.090	0.98	0.35	$4.14 \times 10^5$
03	1.196	0.95	0.50	$5.92 \times 10^5$
06	1.617	0.87	0.80	$9.47 \times 10^5$

TABLE 2. Jet flow conditions for setpoints 01, 03 and 06 based on nozzle pressure ratio (NPR), acoustic Mach number  $M_a$  and Reynolds number  $Re$ .

between the plate trailing edge and the nozzle exit plane, and the height  $h$  as the radial position with respect to the jet centreline. The simulated cases are listed in table 1, marked with an X. For a given flat-plate length, the minimum radial position is determined based on a jet spreading angle of  $7^\circ$  (Brown & Bridges 2006) to avoid grazing flow on the surface. The plate is 12.7 mm thick and it has a chamfer angle of  $40^\circ$  at the trailing edge. It extends  $0.75D_j$  upstream of the nozzle exit plane to avoid scattering effects at the leading edge. In the spanwise direction, the plate has a width of  $36D_j$  to avoid side-edge scattering.

The simulated flow conditions are based on setpoints 01, 03 and 06 from the NASA wind tunnel experiments (Brown & Bridges 2006). All setpoints are characterized by subsonic jets with different acoustic Mach numbers ( $M_a = U_j/c_\infty$ ). The jet flow characteristics are included in table 2, such as the nozzle pressure ratio (NPR), the temperature ratio  $T_R$  (ratio between the jet and ambient static temperatures) and the Reynolds number  $Re$ , based on the nozzle exit diameter. Static flow parameters, such as ambient pressure and temperature, are taken from the work of Brown & Bridges (2006).

### 3.2. Computational set-up

The jet and the flat plate are placed in an almost quiescent domain, i.e. with a speed equal to 1% of the jet exit velocity, at ambient pressure. This free-stream



condition is added to avoid the situation in which eddies escaping the jet shear layer are trapped in the domain and do not dissipate, allowing the solver to operate and converge faster. This free-stream speed is considered negligible, compared to the jet velocity, and thus it does not alter the flow-field characteristics of the shear layer and the far-field noise. To generate the jet flow, an additional inlet boundary condition is placed  $8D_j$  upstream of the nozzle exit plane (figure 1). The physical parameters used as boundary conditions are taken from experimental data (table 2). A zigzag trip, with a thickness of 1 mm ( $0.02D_j$ ) and spacing of 1.62 mm ( $0.03D_j$ ), is added inside the nozzle,  $1.5D_j$  upstream of the exit plane, to force a fully turbulent boundary layer. This nozzle set-up was validated for the isolated jet case by van der Velden *et al.* (2018). The same strategy is adopted in this work for the installed case.

The main components of the set-up are shown in figure 1. A permeable FWH surface, represented by dashed lines, is used for the far-field noise computations. Its shape and dimensions are chosen such that the same surface can be used for all studied configurations. A length of  $22D_j$  downstream of the nozzle exit plane and a width of  $10D_j$  are used for the permeable surface to include all the sources of noise relevant for the current investigation.

Spurious effects due to hydrodynamic pressure fluctuations occurring on the FWH are avoided by placing cutouts at the nozzle and flat-plate regions. Additional sources caused by the jet crossing the downstream end of the FWH are mitigated by placing seven outflow surfaces (or end caps) at that region (figure 1). The far-field pressure signals obtained from each cap (located at different streamwise positions) are averaged, so that the spurious noise produced by the eddies crossing the permeable surface can be removed from the final far-field spectra (Brès *et al.* 2012).

Acoustic sponges, which consist of regions of increased viscosity, are added to the set-up in order to prevent wave reflection at solid boundaries and at the walls of the computational domain (Colonus, Lele & Moin 1997). Inside the nozzle, the sponge extends from the inlet plane up to  $3.8D_j$  upstream of the exit plane. A spherical sponge with a diameter  $130D_j$ , centred at the nozzle exit plane and encompassing the entire geometry, is also added. A progressive coarsening of the grid towards the boundaries also contributes to the dampening of reflected acoustic waves.

The physical time of the simulations is divided into an initial transient, consisting of 10 flow passes through the FWH surface, and an acquisition time of 13 flow passes (total simulation time of 23 flow passes). The latter is defined based on the minimum output frequency to be analysed (defined as  $St = 0.04$ ), and the number of spectral averages (defined as 20), for an overlap coefficient of 0.5 in the fast Fourier transform (FFT) computation. For the finest grid resolution investigated, the physical time step is  $1.5 \times 10^{-7}$  s for all setpoints, and the unsteady pressure on the FWH surface is sampled with a frequency of 416 kHz. The resultant physical simulation time and acquisition parameters are shown in table 3. The frequency resolution refers to the frequency band obtained from the FFT of the computed acoustic signals, based on the acquisition time and the selected number of averages.

Similarly as performed in the NASA benchmark experiments (Brown 2012), the far-field noise levels are computed with a microphone arc array. The array is centred at the nozzle exit plane, with a radius of  $100D_j$ . Microphones are placed at an interval of  $5^\circ$ , ranging from  $\theta = 50^\circ$  to  $\theta = 165^\circ$  ( $\theta = 180^\circ$  corresponds to the jet axis). The noise levels are evaluated at both shielded and reflected sides of the plate, as shown in figure 2(a). An additional azimuthal array is located around the nozzle exit plane, normal to the jet axis, with 12 microphones spaced of  $30^\circ$ , as shown in figure 2(b).



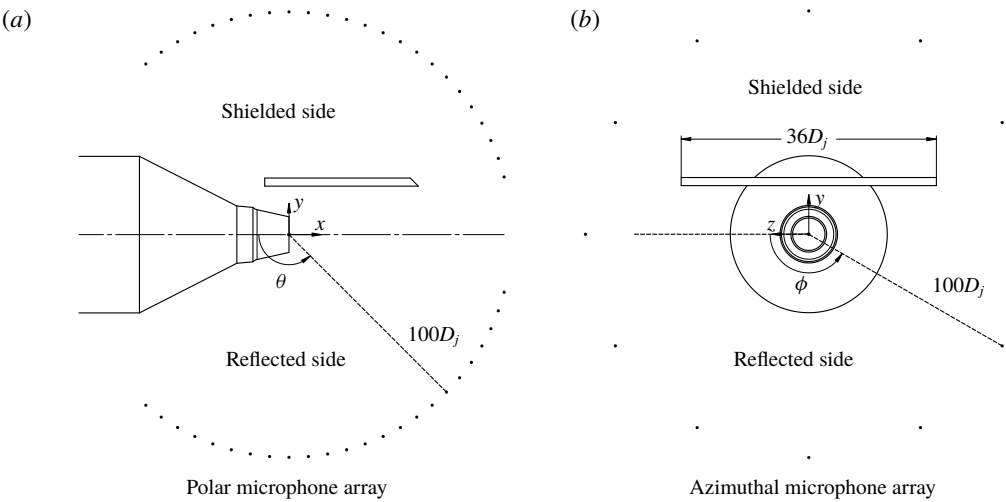


FIGURE 2. Far-field microphone positions: (a) 48 microphones in the polar array, divided for the reflected and shielded sides; (b) 12 microphones in the azimuthal array, normal to the jet axis. Microphone distances not to scale.

Setpoint	Physical simulation time (s)	FWH acquisition time (s)	Frequency resolution (Hz)
01	0.221	0.16	63
03	0.198	0.11	91
06	0.081	0.07	143

TABLE 3. Simulation physical time and acquisition parameters for each setpoint.

Grid	Resolution	Voxel size at nozzle exit and jet plume (mm)	Finest voxel size (mm)	Number of voxels ( $10^6$ )	kCPUh
Coarse	32	1.588	0.1985	153.2	5.5
Medium	45	1.129	0.1411	371.2	23
Fine	64	0.794	0.0992	942.4	48

TABLE 4. Grid characteristics for convergence analysis.

#### 4. Grid convergence and validation

A mesh convergence study is performed to assess the sensitivity of the numerical results to the discretization of the computational domain. The mesh resolution is defined as the number of voxels at the nozzle exit diameter. The resultant element size is used throughout the jet plume. Three grids are investigated: coarse (resolution = 32 voxels/ $D_j$ ), medium (resolution = 45 voxels/ $D_j$ ) and fine (resolution = 64 voxels/ $D_j$ ). The features of each grid are summarized in table 4. Details of the mesh set-up are reported in van der Velden *et al.* (2018).

The isolated and installed ( $L = 4D_j$  and  $h = 1D_j$ ) configurations, in the conditions of setpoint 03 ( $M_a = 0.5$ ), are used for the flow-field convergence study. The chosen

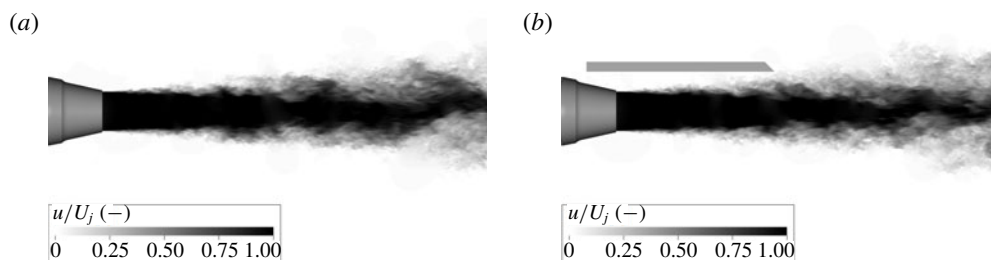


FIGURE 3. Snapshots of the instantaneous flow field for (a) isolated and (b) installed jet configurations ( $L=4D_j$  and  $h=1D_j$ ). No visible change to the jet development is caused by the plate.

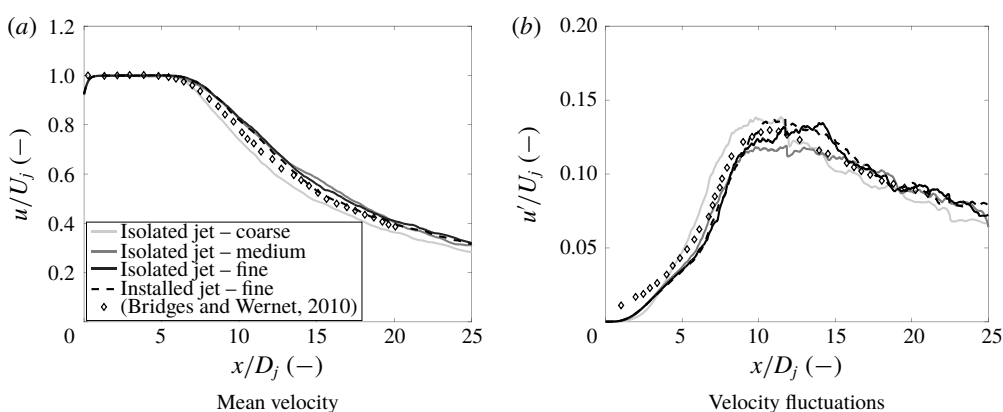


FIGURE 4. Profiles of (a) time-averaged and (b) r.m.s. of fluctuations of the axial velocity component at the nozzle centreline for different grid resolutions, and compared to experimental data for setpoint 03.

installed case represents the configuration for which the surface is closest to the plume. Results are also compared with experimental data from Bridges & Wernet (2010) for validation. Flow-field measurements from particle image velocimetry are available for the isolated jet case (Bridges & Wernet 2010). The absence of hydrodynamic interaction between the jet flow and the solid surface allows the use of these results for validation of all configurations. As can be appreciated from both the instantaneous flow realizations for the isolated and installed jet cases in figure 3, and the time-averaged velocity profiles and root mean square (r.m.s.) of velocity fluctuations in figure 4, no significant difference between isolated and installed configurations is found in either the jet-flow field or the centreline velocity profiles.

From figure 4, it is shown that the potential core is well captured, compared to the experimental results, extending up to  $6.5D_j$  from the exit plane. A small over-prediction of the velocity decay at the centreline, of the order of  $0.04U_j$ , is also found. Minor deviations in velocity amplitude are also seen between the medium and fine isolated cases around  $12 < x/D_j < 15$ , probably due to the strong unsteadiness of the flow in that region. Similarly, both the amplitude and the spatial development of the turbulent velocity fluctuations are well captured, with minor differences between the three grids and the experimental results. It is conjectured that these small deviations

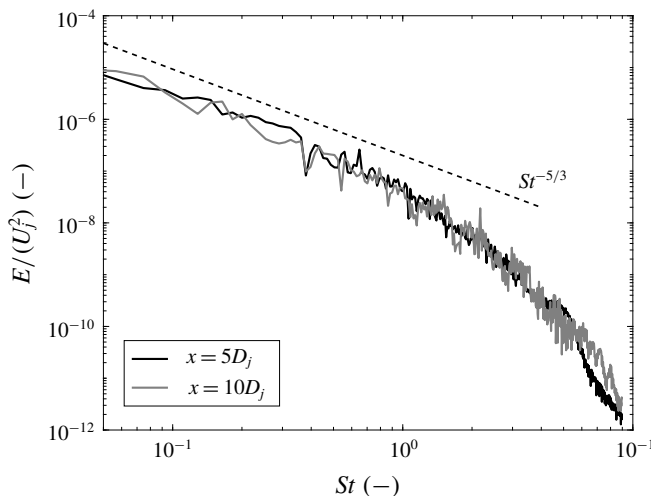


FIGURE 5. Spectra of turbulent kinetic energy for two probes at the nozzle lipline ( $y = 0.5D_j$ ) of the isolated jet (setpoint 03).

in the velocity r.m.s. occur due to the turbulence properties set at the nozzle inlet, which do not match perfectly the experimental conditions.

A key element for assessing the quality of the simulation is that turbulence in the mixing layer is accurately resolved in the frequency range of interest. The spectrum of turbulent kinetic energy  $E$  versus Strouhal number ( $St = f \times D_j/U_j$ ), obtained for setpoint 03, is shown in figure 5 for two probes placed at the nozzle lipline ( $y = 0.5D_j$ ) of the isolated jet, at positions  $x = 5D_j$  and  $x = 10D_j$ . The spectra are shown to follow Kolmogorov's 5/3 decay law up to high frequencies, of the order of  $St = 2$  (6.7 kHz). These results indicate that the turbulence characteristics are correctly modelled and the resultant spectral analyses, including the far-field noise resultant from turbulent mixing, are reliable.

The far-field spectra for the installed configuration are compared to the experimental results from Brown (2012). For the comparisons, an intermediate case ( $L = 4D_j$  and  $h = 1.25D_j$  at setpoint 03) is chosen. The narrowband sound pressure level (SPL), obtained for a constant frequency band of 100 Hz, is plotted against the Strouhal number in figure 6. Results are displayed for the reflected side of the plate (refer to figure 2a), at two polar angles:  $\theta = 90^\circ$ , i.e. the sideline direction, and  $\theta = 150^\circ$ , i.e. near the direction of the jet axis. A reference pressure of  $2 \times 10^{-5}$  Pa is used for the conversion to decibels (dB). The frequency band of the experimental data has also been changed from 12.2 Hz to 100 Hz, so that it is comparable with the simulation results.

The spectral shape is correctly predicted by the simulations from all grids, at both polar angles. At low and mid-frequencies, the curves for the medium and fine grids display similar amplitudes, and convergence is achieved. For high frequencies, the effect of grid resolution is more evident, and it is related to the cutoff frequency. For the coarse mesh, the cutoff frequency occurs at  $St \approx 1.8$ , whereas, for the fine case, it occurs at  $St \approx 3$ , based on the chosen element sizes. At frequencies higher than  $St = 3$ , there is less agreement between the numerical (fine case) and experimental results, probably due to grid resolution effects. Up to this frequency, which is the range of interest, the maximum deviation between the results of the fine mesh and

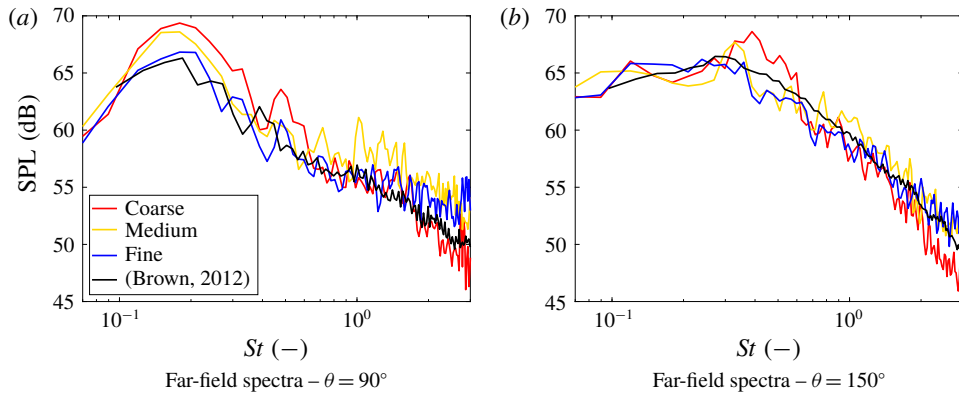


FIGURE 6. Grid convergence and validation of aeroacoustic results for the installed jet ( $L=4D_j$  and  $h=1.25D_j$ ). Spectra obtained for the reflected side of the plate at (a)  $\theta=90^\circ$  and (b)  $\theta=150^\circ$  and setpoint 03.

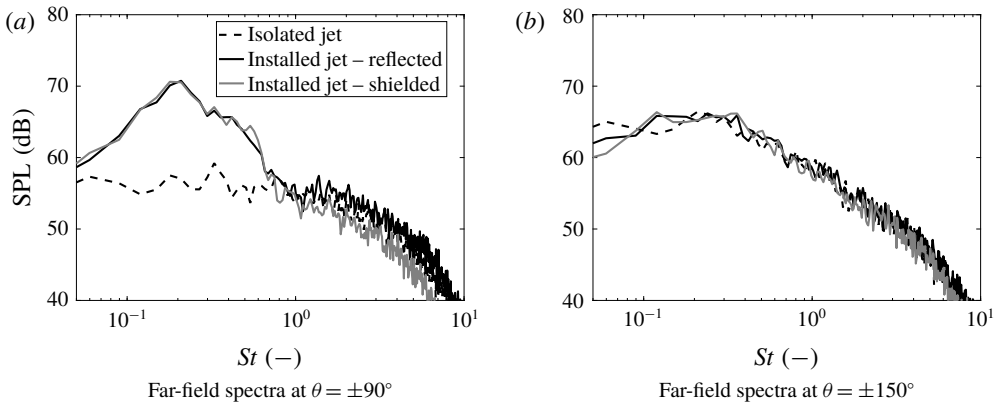


FIGURE 7. Far-field spectra of the installed jet ( $L=4D_j$  and  $h=1D_j$ ), at the reflected and shielded sides of the plate, at (a)  $\theta=\pm 90^\circ$  and (b)  $\theta=\pm 150^\circ$ , compared to the isolated configuration (setpoint 03).

the experiments is approximately 4 dB. This shows the capability of the model to correctly predict JIN with sufficient accuracy. The results shown in the next sections of this paper are therefore obtained from the fine resolution grid so that analyses can be performed up to high frequencies ( $St < 3$ ).

## 5. Installation effects and trailing-edge scattering

The far-field SPL for the isolated and installed jets ( $L=4D_j$  and  $h=1D_j$ ) at setpoint 03 are plotted versus the Strouhal number in figure 7. The spectra are obtained for a constant frequency band of 100 Hz, and at polar angles  $\theta = \pm 90^\circ$  and  $\theta = \pm 150^\circ$ .

In the sideline direction ( $\theta = \pm 90^\circ$ ), installation effects result in low-frequency noise amplification, up to  $St = 0.7$ . The maximum increase, relative to the isolated case, is 14 dB at  $St = 0.19$ . In the frequency range  $0.05 < St < 0.7$ , the spectra at the reflected and shielded sides display similar shape and amplitude, in agreement with Head & Fisher (1976). This confirms that, for this frequency range, the dominant

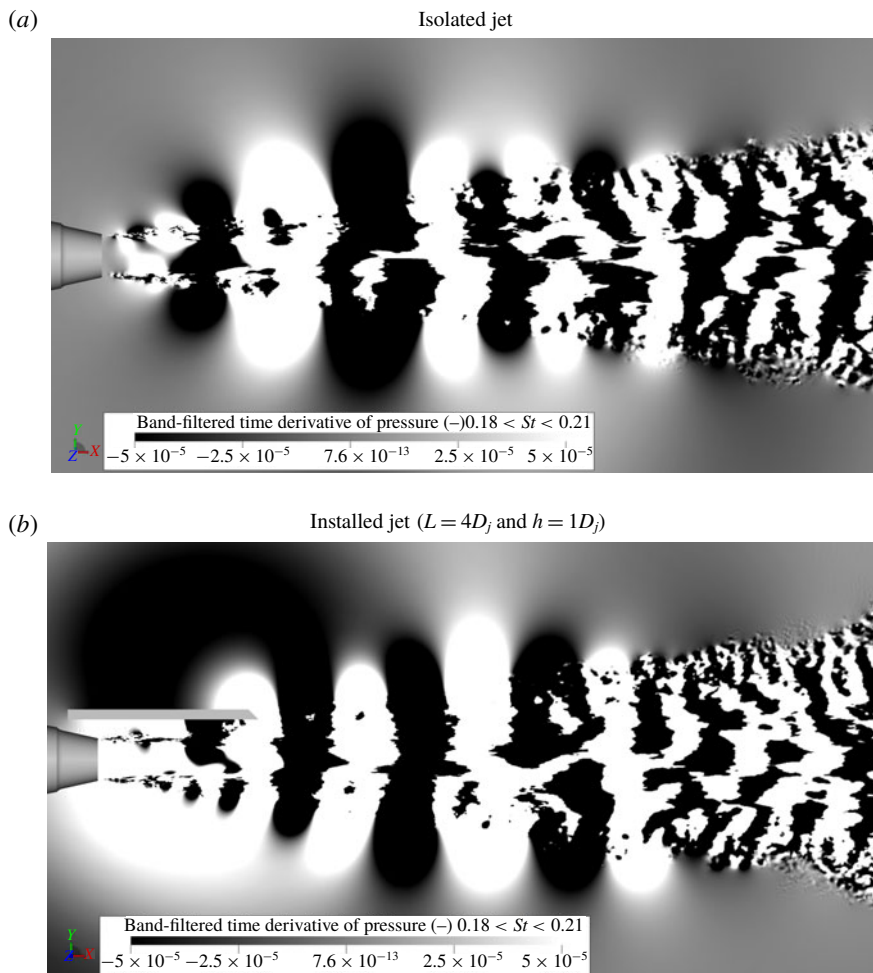


FIGURE 8. Contours of the time derivative of the pressure field of isolated and installed jets, bandpass-filtered over a frequency range  $0.18 < St < 0.21$ . Contours are saturated so that pressure waves outside of the jet plume can be identified.

noise generation mechanism is the scattering of the near-field hydrodynamic waves at the trailing edge of the flat plate. For  $St > 0.7$ , the spectra for the installed cases are dominated by quadrupole noise sources. At the reflected side, noise levels are approximately 3 dB higher than those of the isolated case, as expected from the reflection on a half-plane (Cavalieri *et al.* 2014). For  $\theta = \pm 150^\circ$ , i.e. towards the jet axis, installation effects are no longer visible and the spectra are similar to that of the isolated jet.

To determine the dominant noise sources for each configuration, instantaneous dilatation field contours for the jet at setpoint 03 are shown in figure 8(a,b). They are obtained for a frequency band of  $0.18 < St < 0.21$ , corresponding to the region of maximum noise increase due to installation effects. Contours are saturated so that pressure waves outside of the jet plume can be identified.

For the isolated case, the dilatation field shows pressure waves convecting with the jet. Given the low Mach number investigated ( $M_a = 0.5$ ), it is expected that

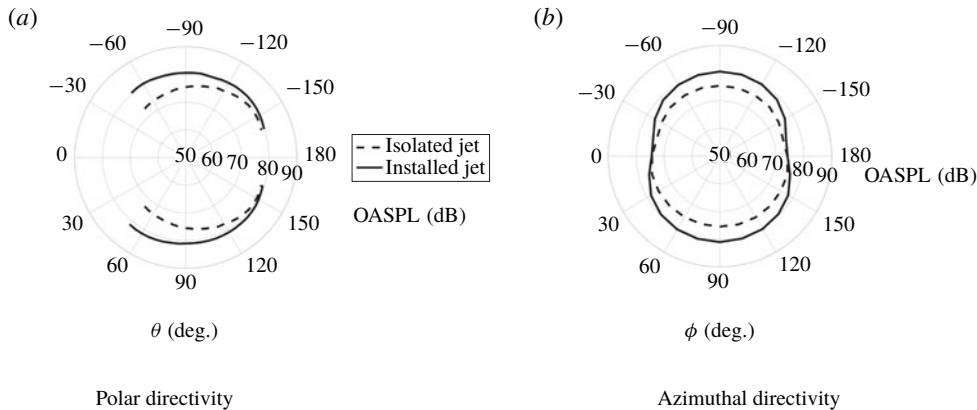


FIGURE 9. (a) Polar and (b) azimuthal directivities of the isolated and installed jets ( $L = 4D_j$  and  $h = 1D_j$ ) for setpoint 03.

a large portion of those waves convect at subsonic speeds. A distinct change of their amplitude, characterized by growth, saturation (peak region) and decay, can be observed. Therefore, due to this spatial modulation, a small portion of the energy of the waves in the evanescent near pressure field propagates to the far field as noise (Jordan & Colonius 2013). For the installed jet, additional acoustic waves are generated due to scattering at the plate trailing edge. Waves on the shielded and reflected sides of the plate have opposite sign, indicating a phase shift of  $\pi$ , as described by Head & Fisher (1976) and Cavalieri *et al.* (2014). These scattered waves then propagate in the upstream direction of the jet.

The previous observations are confirmed by the directivity plots of overall sound pressure level (OASPL), integrated in the range  $0.05 < St < 3$ , shown in figure 9. In the polar direction (figure 9a), the maximum noise increase occurs at  $\theta \approx \pm 50^\circ$ . Smaller angles could not be computed due to the presence of the nozzle, which acts as a shielding body. However, the trend is consistent with the cardioid directivity, proposed by Ffowcs-Williams & Hall (1970). Approaching the jet axis, the curves for the isolated and installed cases collapse, confirming that the quadrupole sources dominate. In the azimuthal direction, the OASPL values are plotted normal to the jet axis, for a fixed polar angle of  $\theta = 90^\circ$ . The isolated jet displays an axisymmetric behaviour, with similar noise levels at all azimuthal angles. For the installed jet, a maximum noise increase of 5 dB is obtained in the direction normal to the flat plate ( $\phi = \pm 90^\circ$ ), whereas no difference is present for  $\phi = 0^\circ$  and  $\phi = 180^\circ$ . For intermediate angles, a small difference is visible between the upper and lower sides, due to shielding and reflection effects. This directivity pattern is consistent with the presence of acoustic dipoles, with axes perpendicular to the surface, in agreement with Head & Fisher (1976).

Spectra of surface pressure fluctuations for probes placed at the trailing edge and leading edge of the plate are plotted in order to verify that trailing-edge noise is the dominant source. The spectra in terms of pressure power amplitude (pressure squared), non-dimensionalized by the square of the jet nominal dynamic pressure ( $q = 0.5\rho U_j^2$ ), are shown in figure 10. There is a large difference in amplitude between the curves, of approximately three orders of magnitude. This indicates that there are no significant hydrodynamic fluctuations at the leading edge, and, consequently, scattering at the leading edge has minor effects on the overall acoustic field.

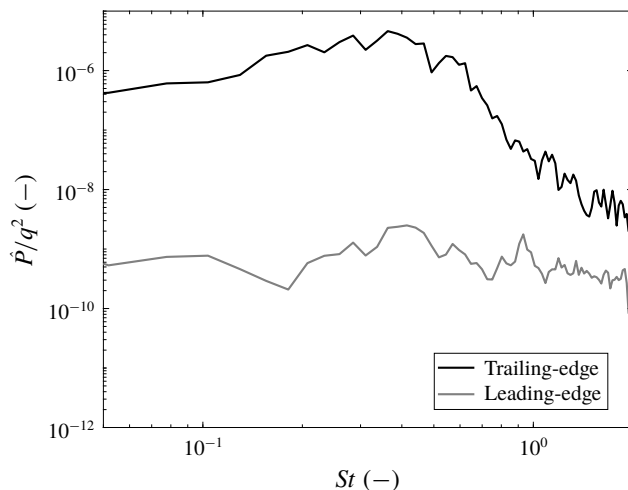


FIGURE 10. Far-field spectra of pressure fluctuations on probes at the leading and trailing edges of the plate, at the jet symmetry plane, obtained for setpoint 03.

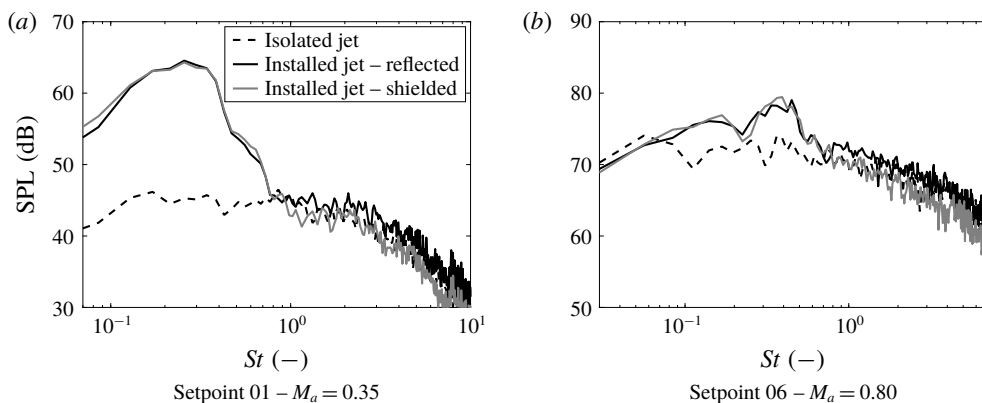


FIGURE 11. Far-field spectra of the installed jet ( $L=4D_j$  and  $h=1D_j$ ), at the reflected and shielded sides of the plate, compared to the isolated configuration for (a) setpoint 01 ( $M_a=0.35$ ) and (b) setpoint 06 ( $M_a=0.80$ ), for polar angles  $\theta = \pm 90^\circ$ .

The sound pressure levels of the installed jet ( $L=4D_j$  and  $h=1D_j$ ) for the other setpoints are plotted with the respective isolated configuration spectra in figure 11, for polar angles  $\theta = \pm 90^\circ$ . For the low-Mach-number jet ( $M_a=0.35$ ), shown in figure 11(a), a strong amplification occurs at low frequencies, similar to the previous results for setpoint 03. At the spectral peak ( $St=0.26$ ), there is a difference of 19 dB between installed and isolated noise levels. The spectra for shielded and reflected sides show similar values up to  $St=0.77$ , which marks the maximum frequency for which the scattering at the trailing edge is the dominant source. For the high-Mach-number case ( $M_a=0.8$ ), installation effects result in a lower amplification with respect to the isolated case at the spectral peak (5 dB at  $St=0.4$ ). This is due to the dependence of the sound intensity with the jet velocity, which is  $U_j^5$  for the scattering (Ffowcs-Williams & Hall 1970) and  $U_j^8$  for turbulence-mixing noise (Lighthill 1952). Therefore, with a high-velocity jet, the spectrum is dominated by the isolated jet noise due to turbulent mixing.



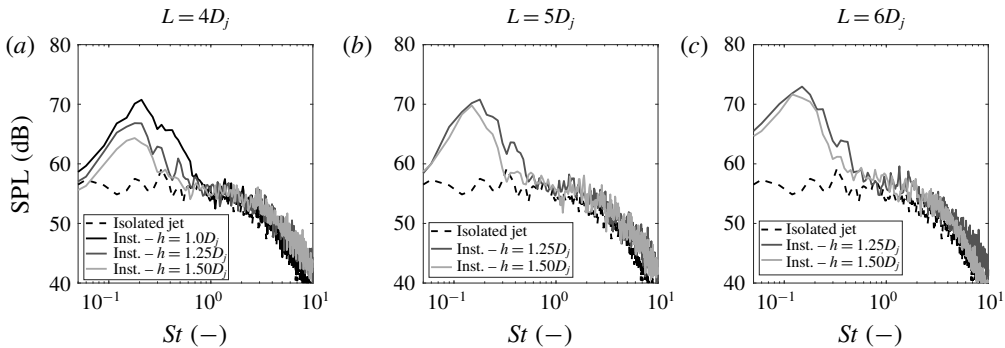


FIGURE 12. Effect of changing the plate radial position on the far-field noise levels. Spectra are plotted for different plate lengths of (a)  $L = 4D_j$ , (b)  $L = 5D_j$  and (c)  $L = 6D_j$ , at a polar angle  $\theta = 90^\circ$  (reflected side) and for  $M_a = 0.5$ .

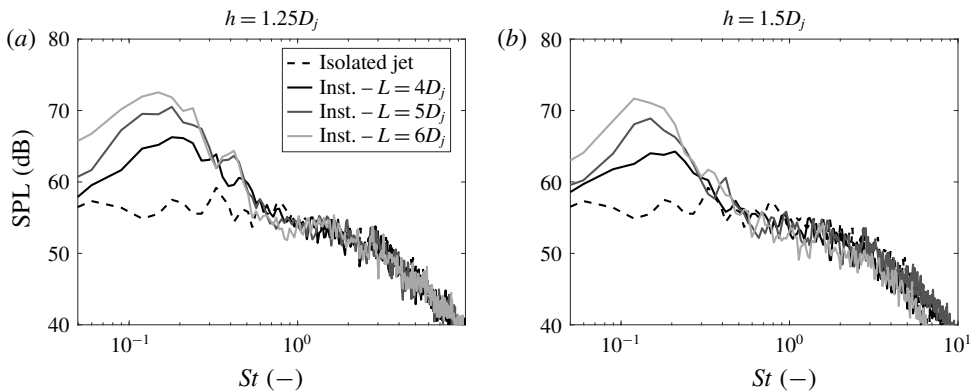


FIGURE 13. Effect of changing the plate length on the far-field noise levels. Spectra are plotted for different plate heights of (a)  $h = 1.25D_j$  and (b)  $h = 1.50D_j$ , at a polar angle  $\theta = -90^\circ$  (shielded side) and for  $M_a = 0.5$ .

The influence of the solid plate geometry on the installed far-field noise is also assessed. Results pertaining to the change of the plate radial position relative to the jet centreline are shown in figure 12, for the three investigated plate lengths and  $M_a = 0.5$ . The spectra, plotted for  $\theta = 90^\circ$  (reflected side of the plate), show that moving the surface away from the plume results in lower noise levels, especially at mid-frequencies. For the case with  $L = 4D_j$ , there is a decrease of 4 dB between  $h = 1D_j$  and  $h = 1.25D_j$ , and 6 dB between  $h = 1D_j$  and  $h = 1.50D_j$  at the spectral peak ( $St = 0.2$ ). Similar trends occur for other plate lengths and jet setpoints. The cross-over point with respect to the isolated jet curve also moves to higher frequencies for surfaces closer to the jet. For  $L = 4D_j$ , the cross-over shifts from  $St = 0.33$  ( $h = 1.50D_j$ ) to  $St = 0.70$  ( $h = 1D_j$ ). This is probably due to the increased proximity of the surface to smaller-scale eddies that generate higher-frequency noise when scattered.

The effect of changing the plate length is shown in figure 13. Spectra are obtained for three surface lengths, at fixed radial positions  $h = 1.25D_j$  and  $h = 1.50D_j$ , for  $\theta = -90^\circ$  and  $M_a = 0.5$ . It is shown that, for longer surfaces, noise increase is higher at low frequencies, with a difference of 7 dB between the curves for  $L = 6D_j$  and  $L = 4D_j$ , for  $h = 1.25D_j$  and  $St = 0.15$ . For longer plates, the spectral

peak also moves towards lower frequencies: for  $h = 1.25D_j$  the spectral peak is at  $St = 0.18$  and  $0.15$  for the shortest and longest plates, respectively. This is due to the increase of energy content of large-scale structures in the mixing layer in the downstream direction of the jet (Lawrence *et al.* 2011). Since these structures generate low-frequency hydrodynamic pressure waves, the scattering effects are also amplified in that frequency range. At frequencies higher than  $St = 0.2$ , the difference between the curves is small, and the cross-over frequency with the isolated curve is not significantly changed for different plate lengths. At high frequencies, the scattering is not strongly affected by changing the surface length since small-scale structures show similar characteristics and amplitude in the streamwise direction (Arndt *et al.* 1997).

The results show that the far-field noise of the installed case is dependent on the characteristics of the near field of the jet and the position of the trailing edge. The phenomena behind JIN are therefore investigated in the next sections, linking the edge scattering phenomenon with jet near-field properties at the trailing-edge region.

## 6. Effect of source characteristics on jet-installation noise

The goal of this section is to identify the frequency range in which JIN is the dominant noise source, for a given plate length and radial position, starting from near-field data of the isolated jet.

This is performed by making use of the inequalities proposed by Ffowcs-Williams & Hall (1970). They found that, for a half-plane, noise amplification is caused by the scattering of eddies within a wavelength from the edge; this satisfies the inequality  $2kr_0 \ll 1$ , where  $k$  is the wavenumber and  $r_0$  is the distance from the centre of the eddy to the edge of the half-plane. On the other hand, for eddies far from the edge, which satisfy the inequality  $(kr_0)^{1/2} \gg 1$ , there is no noise increase due to scattering. These parameters can then be regarded as a measure of source compactness, based on the Helmholtz number  $kr_0$ , which is dependent on the distance between the source and the edge. As a consequence, once this distance is known, a wavenumber envelope of flow structures that are effectively scattered at the trailing edge can be found.

To compute the envelope, an equivalent hydrodynamic source distant  $r_0$  from the plate trailing edge is used, for a given wavenumber, as shown in figure 14. It is assumed that this equivalent source is located within the jet mixing layer, positioned at  $(x_{source}, y_{source})$ . The radial position of the source is assumed to be at the nozzle lipline ( $y_{source} \approx 0.5D_j$ ), which corresponds to the centre of the mixing region in the jet shear layer, i.e. the region of maximum amplitude of hydrodynamic fluctuations (Arndt *et al.* 1997). In more detail, the hypothesis assumes that small changes in the radial position of the equivalent source (around the lipline) are negligible with respect to the distance from the edge. The remaining variable,  $x_{source}$ , is determined by using the near-field pressure spectra of the isolated jet (Arndt *et al.* 1997).

Following Arndt *et al.* (1997), the pressure spectrum in the near field of an isolated jet can be divided into three regions (figure 15). At low frequencies, there is an energy-containing region, characterized by amplitude slowly increasing with frequency. This region extends up to the spectral peak, and then it is followed by the inertial subrange, where there is a steep amplitude decay. Finally, there is the acoustic region, where pressure fluctuations of this type are dominant. The intensity of the pressure fluctuations scales as

$$I \propto \rho_0 a_0 U_0^2 (kr_0)^n, \quad (6.1)$$

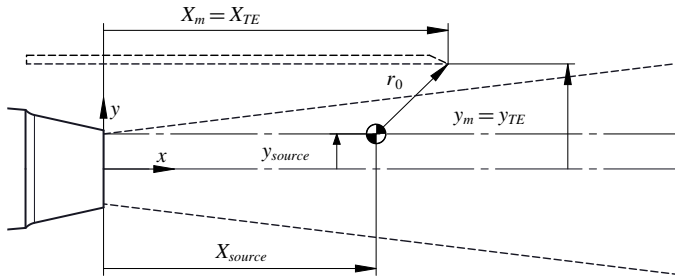


FIGURE 14. Sketch representation of an equivalent source located in the centre of the jet mixing layer (assumed to be the nozzle lipline), at a certain distance  $r_0$  from a defined measurement point (plate trailing edge), for a given wavenumber.

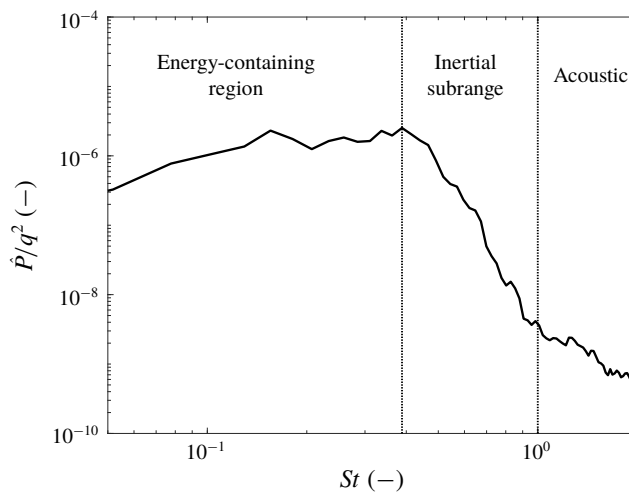


FIGURE 15. Near-field pressure spectrum at  $x = 4D_j$  and  $y = 1.5D_j$ . At low frequencies, the spectrum display amplitudes increasing with frequency up to the spectral peak (energy-containing region), followed by a decay (inertial subrange). At higher frequencies, the pressure fluctuations display acoustic behaviour.

where  $\rho_0$  is the fluid density,  $a_0$  is the speed of sound and  $U_0$  is the source velocity. For the energy-containing region, where the sources display hydrodynamic behaviour,  $n = -6$ . For the inertial subrange,  $n = -6.67$  to take into account the spectral decay with frequency. Finally, when  $n = -2$ , the sources display an acoustic behaviour (Arndt *et al.* 1997).

Since JIN is correlated to hydrodynamic pressure fluctuations (Papamoschou 2010),  $x_{source}$  can be found by fitting the amplitude of pressure fluctuations from a set of near-field spectra of the isolated jet, for a given wavenumber. For a given plate length with the trailing edge located at  $x_m$ , the procedure for the fitting is the following:

- (i) spectra in the near field of the isolated jet dataset are extracted at different radial positions ( $y_m$ );
- (ii) a source position ( $x_{source}$ ) is assumed upstream of  $x_m$ ;

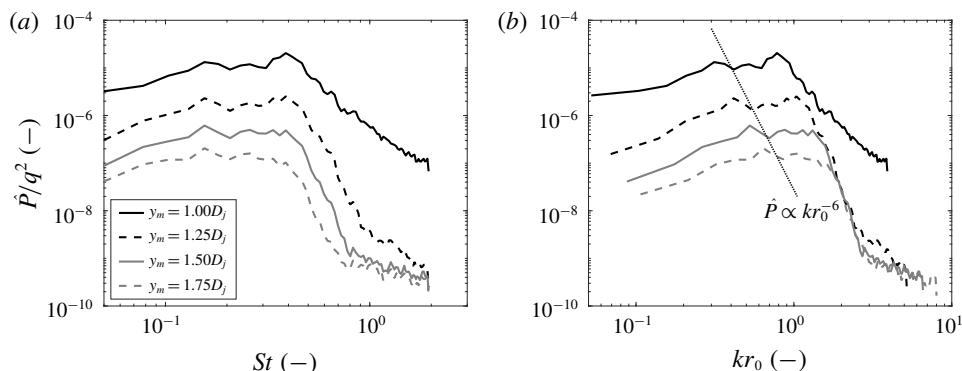


FIGURE 16. Near-field pressure spectra at different radial positions for the calculation of source-edge distance, obtained at  $x = 4D_j$  and  $M_a = 0.5$ . (a) Spectra as a function of Strouhal number. (b) Spectra as a function of the Helmholtz number  $kr_0$ , based on a converged equivalent source position. The thin dotted line represents a  $r_0^{-6}$  (hydrodynamic characteristic) slope on the pressure data for a constant frequency  $St = 0.2$ .

- (iii) the Helmholtz number ( $kr_0$ ) is computed at the radial locations defined in (i), using the source position from (ii);
- (iv) for a given  $St$  chosen as input, the exponent of  $\hat{P} \propto (kr_0)^n$ , i.e. along the  $r_0$  direction, as described in (6.1), is computed; and
- (v) if  $n \neq -6$ ,  $x_{source}$  is shifted and the exponent is recomputed; when  $n = -6$ , the source position is converged.

An example of the method is shown in figure 16(a), where a set of near-field spectra extracted at  $x_m = 4D_j$  and at different radial stations, for setpoint 03 ( $M_a = 0.5$ ), is reported. After a source position is converged for a chosen frequency value, spectra are represented as a function of  $kr_0$ , as shown in figure 16(b). The thin black dotted line represents the slope of  $kr_0^{-6}$ , crossing the points of constant frequency  $St = 0.2$  for each radial position  $y$ . For this specific frequency and measurement point, the axial position of the source is found at  $x_{source} = 0.9x_m$ , or  $x_{source} = 3.6D_j$ . This analysis is then carried out similarly at other frequencies, and for the two other axial measurement positions ( $x_m = 5D_j$  and  $x_m = 6D_j$ ), as shown in figure 17. Similar trends are obtained for the other setpoints ( $M_a = 0.35$  and  $M_a = 0.8$ ).

It is shown that, for increasing frequency, the equivalent source position moves towards  $x_m$  for all analysed cases. These results show that small-scale equivalent sources need to be positioned axially closer to the trailing-edge location in order to generate hydrodynamic pressure fluctuations able to scatter as noise at that point.

The determination of the equivalent source position allows for the computation of an equivalent distance between source and measurement points, which can be used in the compactness analogy defined by Ffowcs-Williams & Hall (1970). The plots in figures 18(a) and 18(b) show the dependence with frequency of the parameters  $2kr_0$  (eddies near the edge) and  $kr_0^{1/2}$  (eddies far from the edge), respectively. Results are included for the three jet setpoints and four geometrical cases. A dotted line is also included to mark the points where the curves are equal to 1. It can be seen that the values of both parameters increase with frequency, for all conditions. For  $M_a = 0.5$  and a case with  $L = 4D_j$  and  $h = 1D_j$ , the condition  $2kr_0$  reaches 1 for a frequency  $St = 0.21$ . For the other cases, this occurs at lower frequencies ( $St \approx 0.17$ ). For the same case,

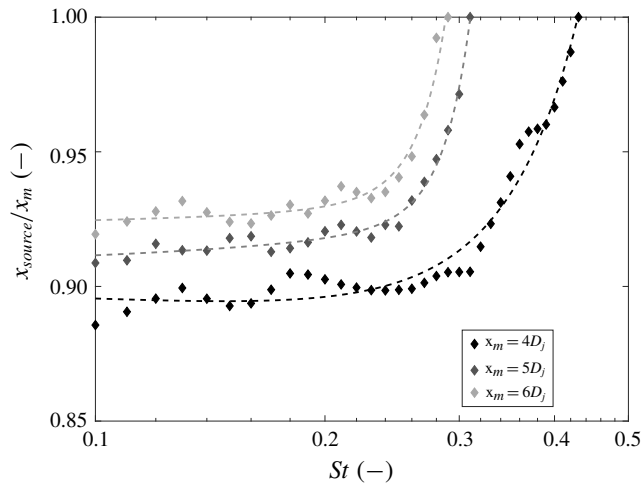


FIGURE 17. Equivalent source position, obtained for different frequencies and axial measurement positions  $x_m$ , for setpoint 03. For increasing frequency, the equivalent source moves towards  $x_m$ .

the other condition  $kr_0^{1/2}$  reaches 1 for a frequency  $St=0.65$  with a similar trend for the other cases. Therefore, it is concluded that there is a frequency range in each case where neither condition defined by Ffowcs-Williams & Hall (1970) is satisfied. In this transition region, a less efficient scattering at the edge (lower sound amplification) is expected due to the structures becoming increasingly compact.

For a better understanding of the physical meaning of these two compactness conditions and how they relate to the produced noise, isolated and installed far-field spectra are plotted in figure 19, highlighting the frequencies where the compactness parameters are equal to 1 with dotted lines. The spectra are obtained for  $M_a=0.5$  at the shielded side of the plate ( $\theta=-90^\circ$ ), for a better visualization of the cross-over frequency between the installed and isolated curves.

The compactness parameters relate to the far-field spectra in two different manners. The frequency limit for eddies very near the edge ( $2kr_0=1$ ) occurs approximately at the location of the peak noise levels for the installed configuration. This is valid for all investigated configurations, and it indicates that the maximum amplification occurs at the limit Helmholtz number where the structures are regarded as non-compact with respect to the edge distance. On the other hand, the frequency limit for eddies far from the edge ( $(kr_0)^{1/2}=1$ ) occurs approximately at the location where the far-field noise levels for the installed configuration cross the curve of the isolated jet. This is consistent with the analytical formulation of Ffowcs-Williams & Hall (1970), which states that eddies far from the edge produce noise levels equivalent to that of free turbulence, when effects of shielding and reflection by the surface are disregarded. Finally, the transition region, where neither inequality is satisfied, is characterized by a decay in noise levels with increasing frequency.

Spectra for two geometric cases, obtained for the other jet setpoints and  $\theta=-90^\circ$ , are plotted in figure 20. Similar trends are obtained for other configurations. The results for  $M_a=0.35$  are in agreement with those obtained previously for  $M_a=0.5$ , where the condition  $2kr_0=1$  occurs at a frequency near the spectral peak, and  $kr_0^{1/2}=1$  occurs near the cross-over between isolated and installed curves. For  $M_a=0.8$ ,

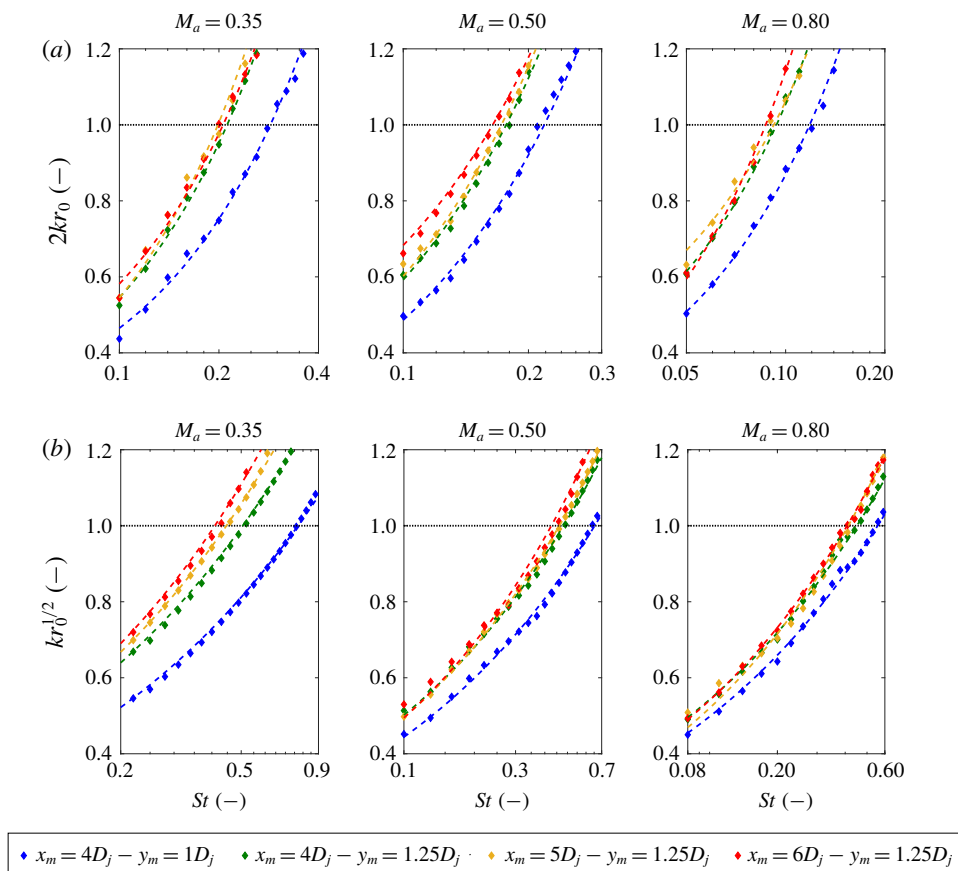


FIGURE 18. Compactness parameters ( $2kr_0$  and  $kr_0^{1/2}$ ) as a function of frequency, obtained for different measurement points at three jet acoustic Mach numbers. A dotted line is included to determine the frequency where these parameters are equal to 1.

however, this approach does not provide the same conclusions. While the cross-over frequency is still predicted fairly accurately, the first condition does not predict the spectral peak ( $St = 0.4$ , for  $L = 4D_j$ ,  $h = 1D_j$ ), but rather a much lower frequency ( $St = 0.12$ ).

To better understand the reasons behind the discrepancy, figure 21 reports spectra for the isolated and installed configurations, at  $\theta = -90^\circ$ , along with those obtained by integrating only the surface pressure fluctuations on the plate using the FWH solid formulation (Ffowcs-Williams & Hawkins 1969). The latter only accounts for dipole sources on the plate, and thus noise from quadrupoles in the jet is disregarded. The spectra are computed on the upper (shielded side) and lower (reflected side) surfaces, separately, as well as considering the entire plate. On the upper side of the plate, two peaks are visible at  $St = 0.12$  and  $St = 0.4$ , with similar amplitudes. The former occurs approximately at the frequency predicted by the method proposed in this section. The second spectral peak, which is dominant on the lower side of the plate, suggests that other sources of sound in addition to trailing-edge scattering might be present.

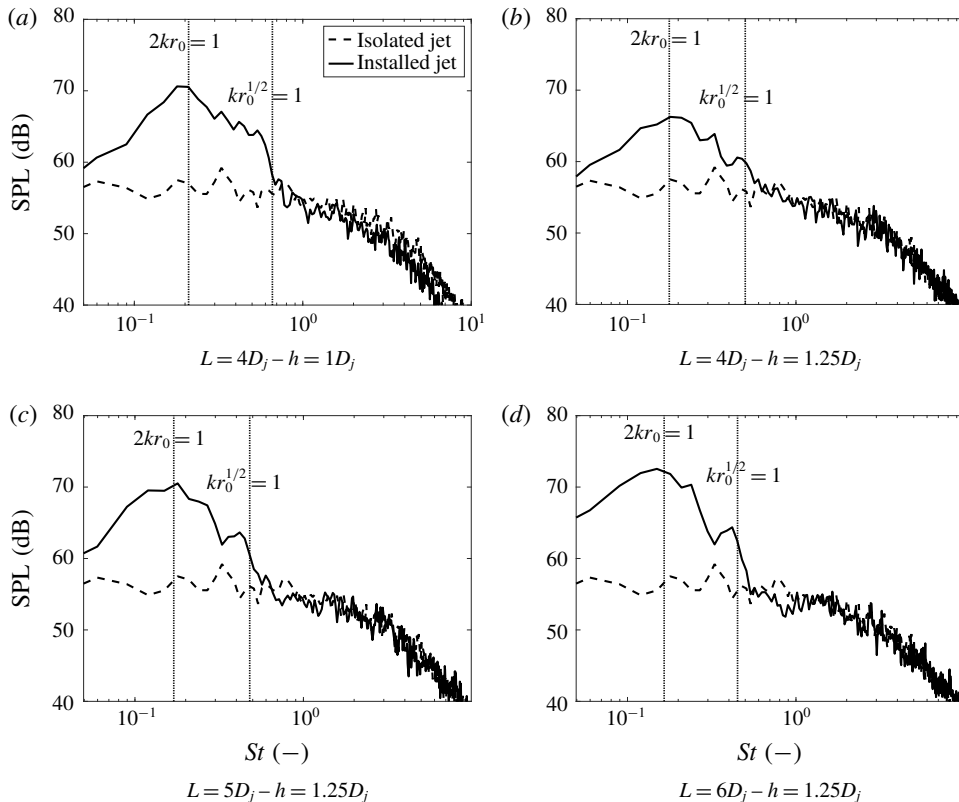


FIGURE 19. Far-field spectra with the frequency values where the compactness parameters  $2kr_0$  and  $kr_0^{1/2}$  are equal to 1, for different plate geometries, as indicated below each panel. The former approaches the peak frequency, whereas the latter approaches the cross-over between installed and isolated curves. Spectra obtained for  $\theta = -90^\circ$  and  $M_a = 0.5$ .

It is concluded that the main characteristics of the frequencies related to JIN are related to the degree of compactness of the sources with respect to their distance to the scattering point. As a reminder, the methodology of this section provides information on the peak frequency of installation effects, as well as the maximum frequency where the trailing edge is the dominant source. This information can be used for assessing installation effects, solely with data from the isolated jet.

## 7. Far-field noise scaling based on near-field properties

In this section, the effect of near-field properties on the spectral amplitude of an installed jet is addressed. This is performed by finding scaling laws for the far-field spectra for different geometric cases, using only information from the isolated jet. Those scaling laws are deemed to predict the far-field noise independently of the geometric configuration adopted for the plate, reducing the need for testing or computing several cases. First, a scaling law is found for moving the plate in the radial direction, and afterwards for changing the plate length.



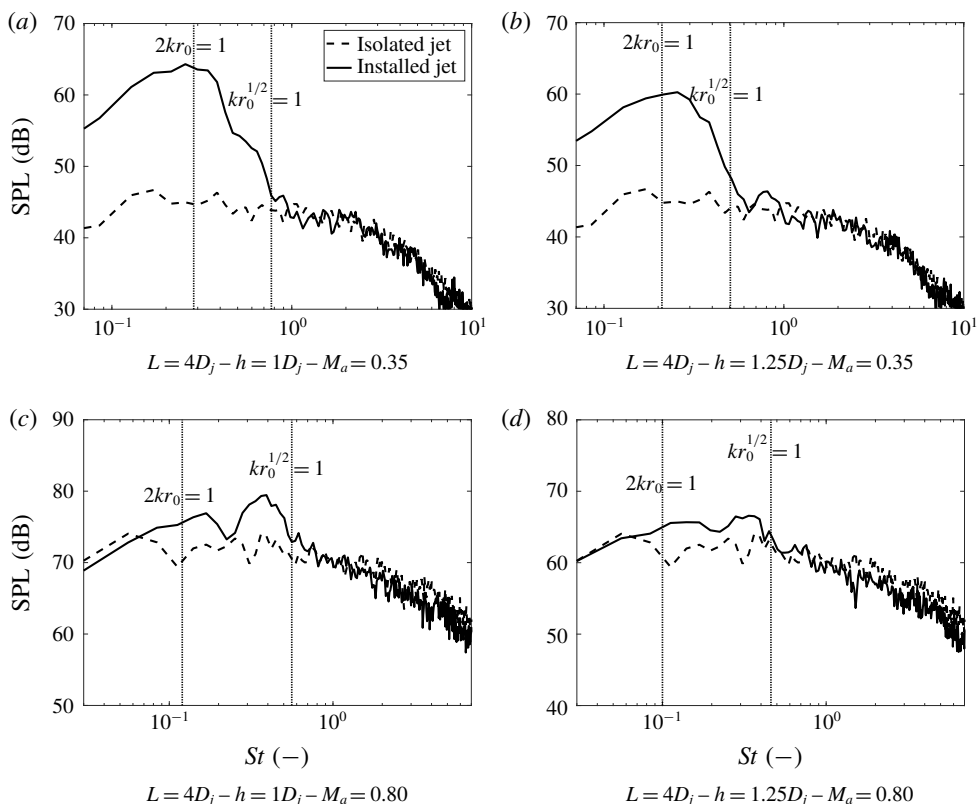


FIGURE 20. Far-field spectra with the frequency values where the compactness parameters  $2kr_0$  and  $kr_0^{1/2}$  are equal to 1, for  $M_a = 0.35$  (a,b) and  $M_a = 0.80$  (c,d). Spectra obtained for  $\theta = -90^\circ$ .

### 7.1. Radial-direction scaling law

The far-field noise data in figure 12 show higher noise levels and a broader frequency range of amplification when the surface is closer to the jet in the radial direction. To relate this behaviour to the near-field characteristics of the isolated jet, spectra of pressure fluctuations from the latter are computed at several locations outside of the plume, similarly as shown in figure 16(a). To determine how the pressure fluctuations for an isolated jet vary in the radial direction, they are plotted against  $y$  in figure 22 for  $M_a = 0.5$ . The curves display the decay at the axial position of  $x = 4D_j$  and frequencies equal to  $St = 0.2$  and  $St = 0.4$  (selected in the noise amplification region for the installed configuration with  $h = 1D_j$ ).

Strong fluctuations occur at  $y = 0.5D_j$ , a location that corresponds to the nozzle lipline. This is in agreement with the assumption made in the previous section that the lipline can be considered the centre of the structures in the mixing layer. Moving away from the jet axis, the near pressure field in the radial direction can be divided into three regions: a nonlinear hydrodynamic field, a linear hydrodynamic field and an acoustic field (Arndt *et al.* 1997). The first one is characterized by the flow inside the plume and nearby regions. Further away from the jet, the hydrodynamic pressure fluctuations display an exponential decay in the  $y$ -direction. For  $St = 0.2$ , the linear hydrodynamic region is placed in the range  $1 < y/D_j < 2.7$ , whereas for  $St = 0.4$  it

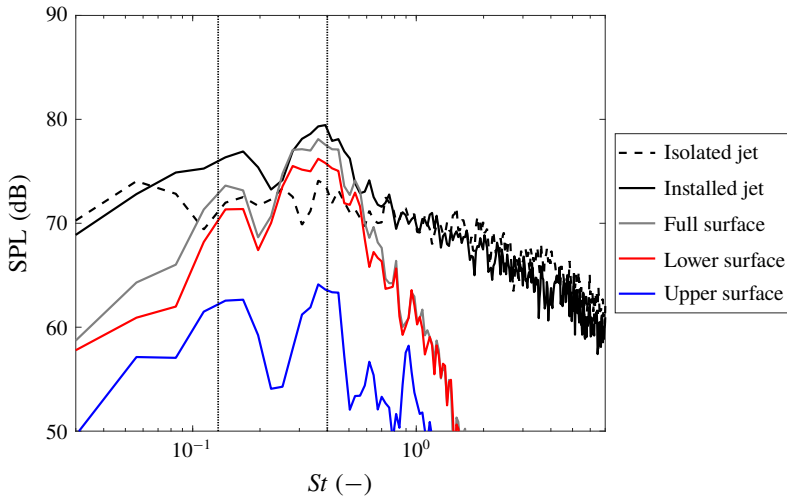


FIGURE 21. Far-field spectra of the isolated and installed jets, with the noise from pressure fluctuations computed on the overall surface, and on the upper and lower sides separately. Spectra obtained for  $\theta = -90^\circ$  and  $M_a = 0.8$ .

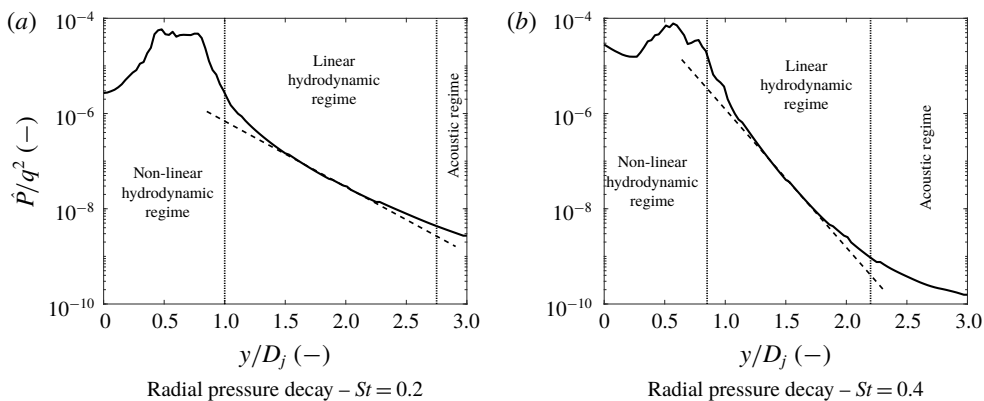


FIGURE 22. Near-field decay of pressure fluctuations in the radial direction for an isolated jet, at  $St = 0.2$  and  $St = 0.4$ , at an axial position  $x = 4D_j$  and for  $M_a = 0.5$ .

occurs closer to the plume, in the range  $0.8 < y/D_j < 2.2$ . Finally, even farther from the jet, pressure fluctuations display acoustic wave characteristics and an algebraic decay (Arndt *et al.* 1997). These results are in agreement with measurements performed in the near field of a jet (Arndt *et al.* 1997; Suzuki & Colonius 2006; Tinney & Jordan 2008). The position and extension of the linear hydrodynamic field, which is the most relevant for this work, are shown to be frequency-dependent. At higher frequencies, the linear decay is steeper and the far field begins closer to the jet. This is consistent with the results from the previous section, where it was shown that small-scale structures become quickly compact when moving away from the lipline. Similar trends are obtained for the other setpoints.

In the linear hydrodynamic region, the pressure fluctuations show an exponential pressure decay. Therefore, the installed far-field noise levels can be scaled with  $e^h$ , based on the respective plate height for each case. This is shown in figure 23(a),

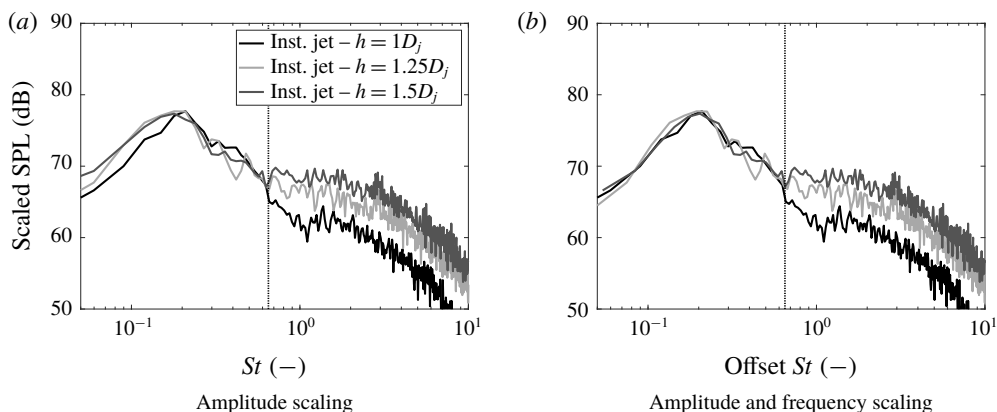


FIGURE 23. Far-field spectra of installed jets, scaled by the exponential of the plate radial position ( $L=4D_j$  and  $\theta=90^\circ$ ), for  $M_a=0.5$ . (a) Only the amplitude of the curves is scaled. (b) The amplitude is scaled and the curves are offset to match the spectral peak.

where there is a fairly good agreement between the curves for  $0.18 < St < 0.65$ . For  $St > 0.65$ , the curves diverge since this region of the spectra is dominated by noise from quadrupole sources reflected on the surface. In the previous sections, it was shown that the spectral peak changes for plates at different radial positions. Therefore, if the scaled spectra are offset in frequency, a better agreement between the curves is found, as shown in figure 23(b). In these plots, the scaled SPL spectra ( $SPL \times e^h$ ) for  $h = 1.25D_j$  and  $h = 1.5D_j$  are offset in frequency ('Offset  $St$ ') so that their peak matches that of  $h = 1D_j$ .

It is then concluded that a combination of amplitude and frequency scaling is necessary to match the noise levels of different radial configurations. While the amplitude can be easily scaled with the exponential of the plate height, knowledge of the spectral peak frequency is necessary beforehand. The method described in the previous section can provide a fairly good prediction of the spectral peak for low/mid-Mach-number jets, and thus it can be used together with the amplitude scaling in order to obtain the far-field spectra of different geometric configurations. This scaling is also applied for plates with different lengths ( $L = 5D_j$  and  $L = 6D_j$ ) as shown in figure 24, with a good agreement between the curves. Scaled spectra for the other jet setpoints are shown in figure 25. For these other conditions there is also a good agreement between the curves. For  $M_a = 0.8$ , however, there is a slight difference in amplitude, particularly at low frequencies ( $St < 0.1$ ), possibly due to effects from sources other than scattering.

## 7.2. Axial-direction scaling law

A similar procedure is carried out to find a scaling law for the noise generated by plates with different lengths. Spectra of near-field pressure fluctuations computed at different axial locations, for  $y = 1.5D_j$  and  $M_a = 0.5$ , are shown in figure 26(a). The results show an increase of low-frequency fluctuations at positions farther from the nozzle exit plane due to the presence of highly energetic large-scale structures. It can be noticed that, aside from  $x = 3D_j$ , the curves tend to collapse at  $St \approx 0.45$ , suggesting that, at high frequencies, the amplitude of the pressure fluctuations remains constant in the axial direction.

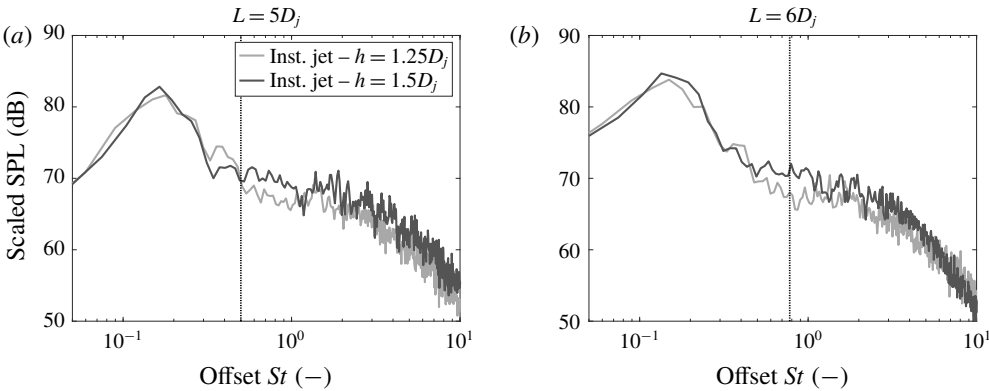


FIGURE 24. Far-field spectra of installed jets, scaled by the exponential of the plate radial position, for  $\theta = 90^\circ$  and  $M_a = 0.5$ . (a)  $L = 5D_j$ , (b)  $L = 6D_j$ .

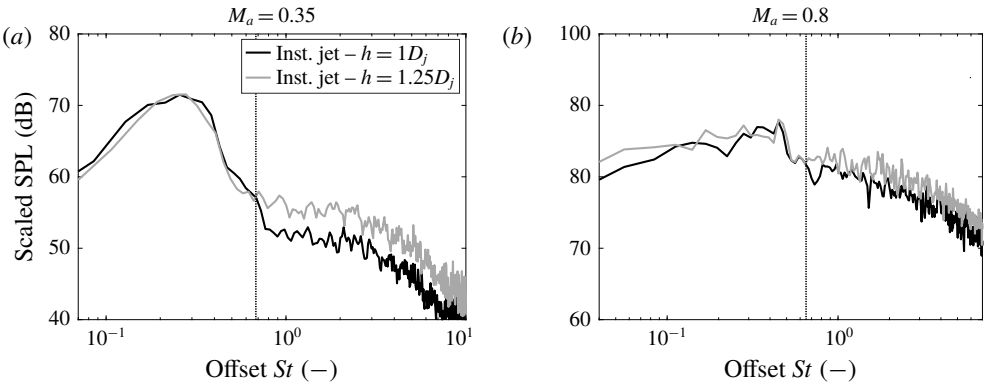


FIGURE 25. Far-field spectra of installed jets ( $L = 4D_j$ ), scaled by the exponential of the plate radial position, for  $\theta = 90^\circ$ . (a)  $M_a = 0.35$ , (b)  $M_a = 0.8$ .

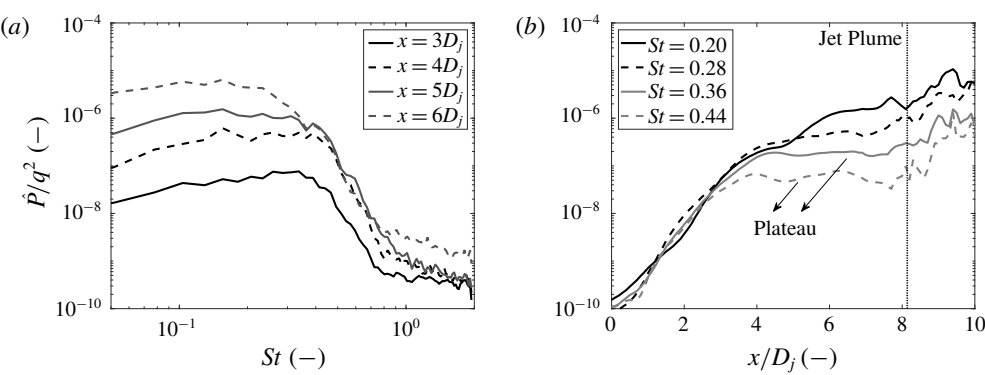


FIGURE 26. (a) Near-field pressure spectra. (b) Progression of near-field pressure in the axial direction. Data obtained for  $y = 1.5D_j$  and  $M_a = 0.5$ .

This behaviour can be better visualized by plotting the amplitude of the pressure fluctuations in the axial direction for specific frequencies (figure 26*b*). At relatively low frequencies ( $St = 0.20$  and  $St = 0.28$ ), the amplitude of pressure fluctuations increases in the axial direction. Owing to the large wavelength associated with these structures, they grow and saturate at positions farther from the nozzle exit plane when compared to small-scale eddies. A nonlinear behaviour is also found downstream of  $x = 8D_j$  due to the presence of the rotational flow inside of the jet plume. At higher frequencies, the amplitude of the pressure fluctuations saturates and remains constant in the axial direction. This plateau is due to the contamination of the signal by the jet acoustic waves (Suzuki & Colonius 2006). If only the coherent, hydrodynamic fluctuations were present, a decay would be expected to follow the saturation point due to the wavepacket nature of the jet (Crighton & Huerre 1990). Therefore, after the saturation point, acoustic fluctuations, which have a slower decay rate, become dominant with respect to hydrodynamic ones.

To remove the contribution of non-coherent fluctuations in the near field, a frequency domain form of POD, known as SPOD, is applied (Schmidt *et al.* 2018; Towne *et al.* 2018), similarly as done in other studies on jet noise (Arndt *et al.* 1997; Tinney & Jordan 2008; Breakey *et al.* 2013). SPOD is preferred to space-only POD because it can properly describe spatiotemporal coherent structures, due to its spectral-based kernel. In this way, the flow is decomposed at different time scales and, consequently, the characteristics of the structures can be analysed for each frequency band (Towne *et al.* 2018), which is necessary for a posterior scaling of the far-field noise. Moreover, due to the segmentation of the signals based on a specified block length, few eigenvectors are obtained and, therefore, few modes are required to reconstruct the wavepacket. On the other hand, to achieve similar results using space-only POD, several modes need to be selected since each of them contains information in the entire frequency range of the analysis. A brief description of the SPOD methodology is reported in appendix A.

The SPOD is applied to the near pressure field of the isolated jet. Data are extracted on a vertical plane crossing the centre of the nozzle. The plane extends  $15D_j$  in the axial direction, relative to the nozzle exit plane, in order to capture low-frequency fluctuations. In the radial direction, the plane extends up to  $2.5D_j$  from the jet centreline. Thus, only the upper half of the jet is considered, enforcing an axisymmetry condition. Based on the available flow-field data of 621 snapshots, eight blocks of 128 snapshots are created, with an overlap of 50 %. A standard Hann window is applied. This allows for the decomposition of the pressure field onto eight independent modes, orthogonal to each other at each computed frequency. The energy content of each mode is plotted in figure 27 for the isolated jet at  $M_a = 0.5$ .

The spectral energy content shown in figure 27 is obtained from the eigenvalues  $\lambda_j(f)$  extracted from the SPOD analysis. The results show a progressive decrease of  $\lambda_j(f)$  for higher mode numbers. The large separation between modes 1 and 2 indicates that the former is dominant and the flow exhibits low-rank behaviour (Schmidt *et al.* 2018). The eigenvectors  $\psi_j(\mathbf{x}, f)$  represent the modal shape. Contour plots in figure 28 represent the shapes of the two most energetic modes at  $St = 0.18$ . The eigenvalues shown above each contour plot represent the fraction of the total energy content for that frequency; the first two modes collect 60 % of the total energy, and mode 1 alone has 36 %. This mode is shown to resemble structures that evolve coherently in space and time. For the remainder of the analysis, only the first SPOD mode is used. Based on the block length selected for the FFT of the near-field pressure data, the wavepacket structures are concentrated in the most energetic mode.

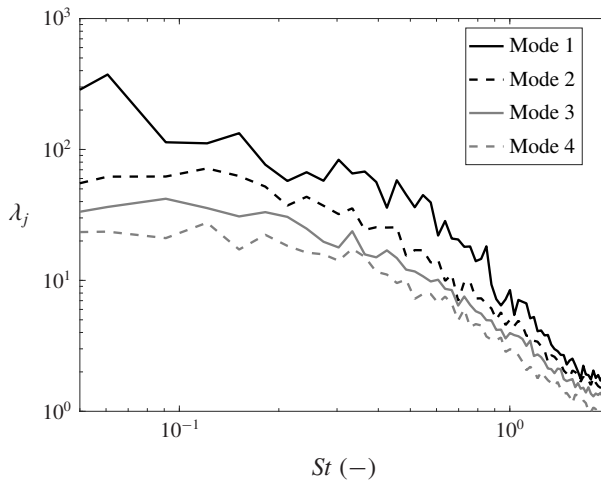


FIGURE 27. Energy content of each SPOD mode as a function of frequency, obtained for  $M_a = 0.5$ .

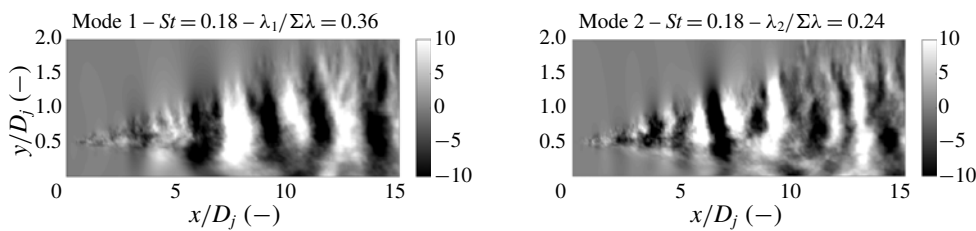


FIGURE 28. First and second SPOD eigenvectors, for a frequency of  $St = 0.18$ , obtained for  $M_a = 0.5$ .

Higher-order modes show a behaviour different from wavepacket-like structures and are disregarded. This is in agreement with analyses by Breakey *et al.* (2013) and Unnikrishnan, Cavalieri & Gaitonde (2019), where the results from the first SPOD mode compare well with analytical methods and experimental data. Therefore, proceeding in the investigation on the behaviour of the structures, the amplitude of mode 1 is then extracted in the axial direction for a fixed height, as shown in figure 29.

The curves in figure 29 display a sinusoidal shape as expected for instability waves or wavepackets. This indicates that SPOD extracts only the coherent part of the pressure field, while the acoustic waves, which cause the plateau in the axial distribution of the pressure fluctuations, are filtered out. It can also be seen that the instability waves start growing at  $x = 2D_j$  in agreement with the results of Suzuki & Colonius (2006). The frequency dependence of mode 1 is shown in figure 29(a). For  $St = 0.18$ , the amplitude of the wave increases in the axial direction, but no saturation or decay is found. At approximately  $x = 8D_j$ , nonlinearities due to the rotational component of the jet flow become significant, as remarked by the modification of the sinusoidal behaviour in the plot. At higher frequencies ( $St = 0.49$ ), growth, saturation and decay occur upstream of the nonlinear region. The spatial dependence in the radial direction, for  $St = 0.18$  (figure 29b), shows a similar trend as the previous

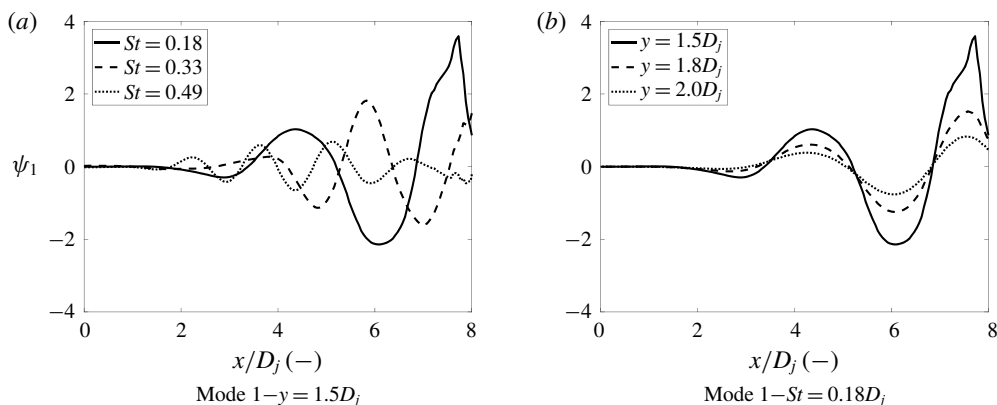


FIGURE 29. Characteristics of SPOD mode 1 in the axial direction, as a function of (a) frequency and (b) radial position. Data obtained for  $M_a = 0.5$ .

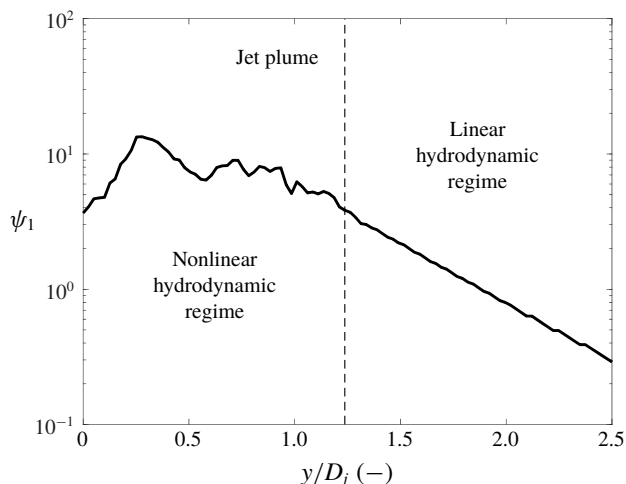


FIGURE 30. Radial decay of SPOD mode 1 for  $x = 6D_j$  and  $St = 0.18$ . Data obtained for  $M_a = 0.5$ .

figure, with an increase in amplitude for locations closer to the jet axis. For a single axial position ( $x = 6D_j$ ), the radial decay is plotted in figure 30, similarly as done in § 7.1. The results are consistent with the ones shown in figure 22, where the hydrodynamic pressure field is divided into linear and nonlinear regions. Therefore, the SPOD analysis confirms the results concerning the exponential pressure decay in the radial direction, described in the previous section.

The spatial modulation of the instability waves, as plotted in figure 29, can be fitted with a Gaussian function (Crighton & Huerre 1990). In figure 31, this fitting procedure is applied to SPOD mode 1 at  $y = 2.0D_j$  for  $St = 0.18$  and  $St = 0.33$ . This height is chosen to avoid contamination of the data by nonlinearities in the jet plume. The Gaussian curves, aside from accurately describing the shape of the instability waves, offer the possibility to approximate the axial behaviour of the pressure fluctuations  $\hat{P}(x, f)$  caused by coherent structures. The width of the Gaussian



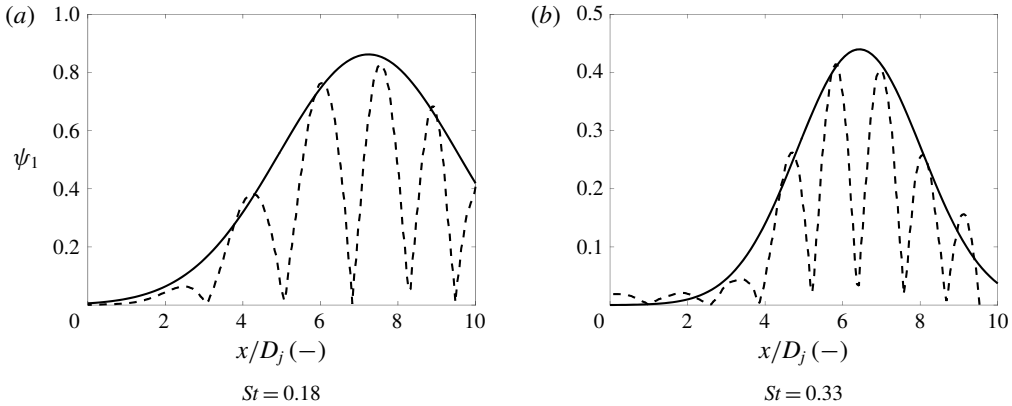


FIGURE 31. Gaussian envelopes around SPOD mode 1, at  $y = 2.0D_j$  for frequencies  $St = 0.18$  and  $St = 0.33$ . Data obtained for  $M_a = 0.5$ .

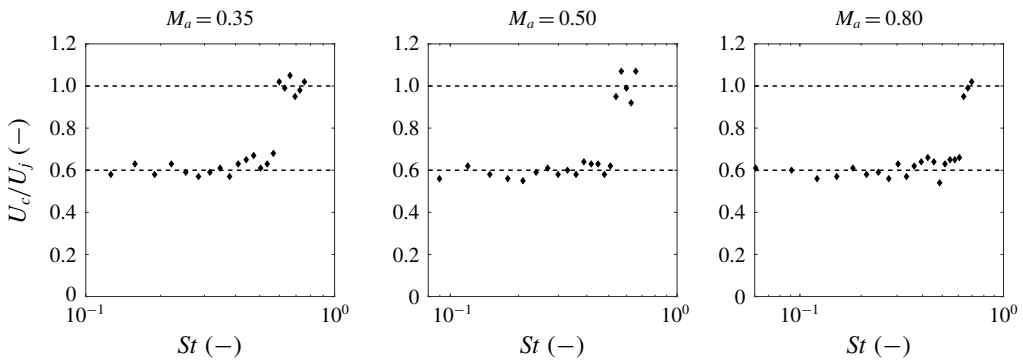


FIGURE 32. Convective velocity ( $U_c$ ) of the structures present in the jet mixing layer, as a function of frequency, obtained from the axial evolution of SPOD mode 1 for three setpoints.

is related to the hydrodynamic wavelength  $\lambda_H(f)$  of the structures, as given by (7.1) (Crow 1972; Laufer & Yen 1983), for a given frequency:

$$\hat{P}(x, f) = \hat{P}_{max}(f) \exp \left[ - \left( \frac{x - x_{max}(f)}{\lambda_H(f)} \right)^2 \right], \quad (7.1)$$

where  $\hat{P}_{max}(f)$  and  $x_{max}(f)$  represent the maximum amplitude of the Gaussian envelope and its axial position, respectively. Therefore, by using (7.1), the hydrodynamic wavelength can be determined for every frequency and, consequently, the convective velocity  $U_c$  of the structures ( $U_c = \lambda_H f$ ). Figure 32 shows the convective velocity for a wide range of frequencies, calculated from the instability waves of SPOD mode 1 at  $y = 2D_j$ . At low frequencies ( $St < 0.15$ ), no results are present due to the nonlinear effects from the plume affecting the data fitting. Similarly, at high frequencies ( $St > 0.7$ ), the quality of the fitting does not allow for conclusions on the hydrodynamic wavelength. In the mid-frequency range, a consistent value of  $U_c \approx 0.6U_j$  is obtained up to  $St = 0.52$ . This is in agreement with the values usually

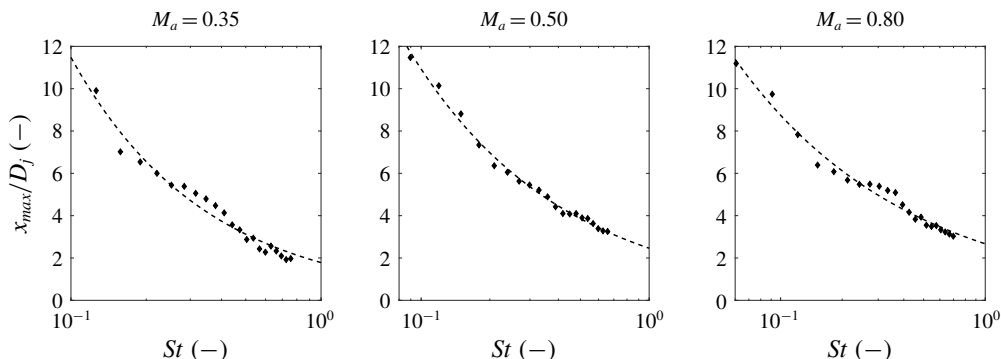


FIGURE 33. Axial position of the Gaussian envelope peak ( $x_{max}$ ), as a function of frequency for three setpoints.

applied in linear stability theory and wavepacket modelling of jets (Papamoschou 2010; Cavalieri *et al.* 2012). The results also agree with those obtained by Arndt *et al.* (1997), who used POD eigenfunctions for the estimation of the convective velocity. For  $St > 0.52$ , a sudden jump is observed, and the convective velocity approximates the nominal jet speed. It is hypothesized that, at the height where this velocity is computed, the pressure fluctuations generated at those mid/high frequencies already display acoustic characteristics (refer to figure 15), and therefore no coherent behaviour can be obtained.

Based on the results of the convective velocity, the SPOD mode 1 represents the coherent hydrodynamic structures in the jet. Given the good agreement of the Gaussian fitting with the axial distribution of pressure fluctuations, equation (7.2) is used for the far-field noise scaling from axial position 1 to axial position 2 (scaled SPL):

$$SPL_{x_1}(f) = SPL_{x_2}(f) \exp \left[ - \left( \frac{x_1 - x_{max}(f)}{\lambda_H(f)} \right)^2 + \left( \frac{x_2 - x_{max}(f)}{\lambda_H(f)} \right)^2 \right]. \quad (7.2)$$

The maximum pressure at each frequency  $\hat{P}_{max}$  is cancelled out when dividing the amplitudes at the two axial positions. Therefore, the only necessary inputs are the hydrodynamic wavelength, which has been calculated along with the convective velocity, and the axial position of the Gaussian peak, which depends on frequency as shown in figure 33 for the three jet setpoints. The positions  $x_1$  and  $x_2$  are considered to be the flat-plate lengths ( $L = 4D_j$ ,  $L = 5D_j$  and  $L = 6D_j$ ), which is consistent with the trailing-edge location for each case.

With all the inputs available, the far-field noise levels of the cases with  $L = 4D_j$  and  $L = 5D_j$  are scaled to a position  $x = 6D_j$  ('Scaled SPL') through (7.2) and plotted against the spectra for the actual case with  $L = 6D_j$ . This is equivalent to dividing the far-field SPL of each installed configuration by the amplitude of the Gaussian at the respective trailing-edge position, for every frequency. These spectra are shown in figure 34, for constant plate heights  $h = 1.25D_j$  and  $h = 1.5D_j$ , and  $M_a = 0.5$ . At low frequencies  $St < 0.06$ , results are omitted since an appropriate Gaussian fitting was not possible due to the limited amount of points available. The scaling in the axial direction is performed only in the frequency range where the convective velocity is equal to  $0.6U_j$  (up to  $St = 0.50$ , as shown by the dotted line).

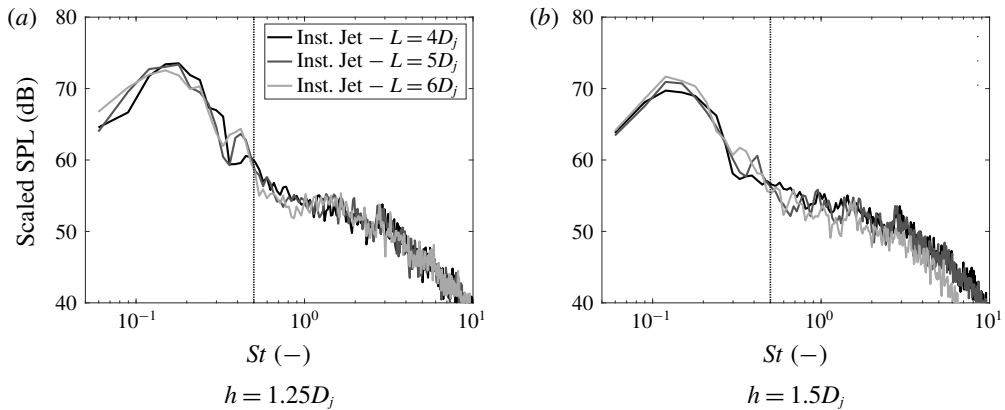


FIGURE 34. Far-field spectra of installed jets for a fixed radial position, scaled from positions  $L = 4D_j$ ,  $L = 5D_j$  and  $L = 6D_j$  through the amplitude of the Gaussian fitting of SPOD mode 1. Spectra obtained for  $\theta = -90^\circ$  and  $M_a = 0.5$ .

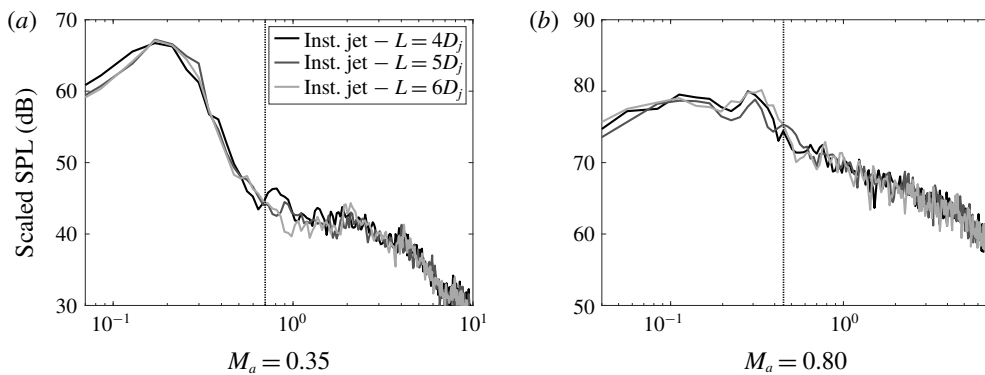


FIGURE 35. Far-field spectra of installed jets for a fixed radial position ( $h = 1.25D_j$ ), scaled from positions  $L = 4D_j$ ,  $L = 5D_j$  and  $L = 6D_j$  through the amplitude of the Gaussian fitting of SPOD mode 1. Spectra obtained for  $\theta = -90^\circ$ .

A good agreement is found for the scaled spectra for both plate heights, with minor deviations for very low frequencies ( $St < 0.1$ ) and when approaching the maximum frequency where  $U_c = 0.6U_j$  ( $St = 0.5$ ). Since the scaling factor is frequency-dependent, the spectral shape for the scaled curves changes, as well as the frequency of the spectral peak. Spectra for the other jet setpoints are shown in figure 35, with a good agreement between the curves as well, indicating that the procedure works for all investigated flow conditions.

The results show that the Gaussian fitting is an adequate parameter for scaling the pressure fluctuations that are scattered by flat plates with different lengths. To obtain this fitting, it is necessary either to have a predicted distribution of coherent structures, or to obtain it *a priori* from a narrow-band analysis of similar coherent structures in the isolated jet flow with a dedicated technique such as SPOD. The results also show that JIN is essentially related to coherent hydrodynamic structures present in the jet mixing layer. The characteristics of these structures determine the far-field noise signature of the installation effects for a given trailing-edge position

(scattering region). The acoustic waves produced by quadrupole sources in the jet do not contribute to installation noise and can be considered uncorrelated to the acoustic dipoles on the surface. With scaling laws found for both radial and axial directions, rapid predictions of JIN can be performed without the need to investigate several geometric configurations. With results from the isolated jet and one installed configuration, the far-field spectra for other plate geometries can be found with relatively good accuracy, thus reducing the need for extensive parametric analyses.

## 8. Conclusions

A high-fidelity numerical investigation of an installed jet is performed using the lattice-Boltzmann method coupled with a very-large-eddy simulation (LBM-VLES). A simplified configuration, comprising a single-stream nozzle and a nearby flat plate, is chosen for the analyses. The simulation results are validated through comparison with experimental data, obtained from tests at NASA Glenn. The far-field spectral results, obtained from the Ffowcs-Williams & Hawkings (1969) (FWH) analogy, indicate a large noise increase at low and mid-frequencies, followed by reflection or shielding of the quadrupole sources, associated with jet noise, at high frequencies. Through dilatation field plots, this amplification is shown to be caused by the hydrodynamic waves generated by the jet that are bounded by the plate and, as they reach a geometric discontinuity (surface trailing edge), they are scattered to the far field as noise. This new source displays a dipolar characteristic in the azimuthal direction, and a cardioid directivity pattern in the polar direction. Maximum noise levels are obtained in the upstream direction of the jet axis, whereas in the downstream direction there is no amplification.

The geometry of the plate also affects the far-field noise. Moving the plate closer to the jet results in higher noise levels, particularly at mid-frequencies, whereas increasing the plate length results in low-frequency noise increase. The different trends in frequency noticed in both radial and axial analyses are then related to the compactness characteristics of the sources. In order to determine the compactness level of a source with respect to a trailing-edge position, two inequalities based on the wavenumber and the relative distance between source and edge are used. For that purpose, the position of the sources must be known beforehand. An equivalent source localization method is proposed by fitting a set of near-field spectra into a decay law, for each frequency of interest. Thereafter, envelopes based on the compactness parameters are determined, which are related to features in the installed far-field spectra. The limit for non-compact eddies agrees with the frequency of the spectral peak, whereas the envelope for compact eddies coincides with the frequency limit of the installation effects. The analysis also yields the existence of a transition region, where neither inequality is satisfied, which is characterized by a progressive decay in amplitude. This method and conclusions are shown to be valid for low/mid-Mach-number jets. For  $M_a = 0.8$ , it is possible that the far-field spectra are dominated by sources other than trailing-edge scattering, and thus the method fails to provide correct information on the spectral peak. Further research into this hypothesis is necessary.

The amplitude of the far-field spectra of the installed cases is also related to the near-field properties through scaling laws. For the radial direction, the plate is placed in the linear hydrodynamic region, where the pressure decays exponentially with increasing radial distance. This characteristic is also visible in the far-field results for the installed case. However, in order to obtain a better agreement, a frequency scaling

is also necessary to match the spectral peak of different configurations. This can be performed using the compactness analysis with an equivalent source. Moreover, this exponential scaling is found to be valid only in the frequency range where the trailing edge is the dominant source.

In order to characterize the hydrodynamic pressure fluctuations along the axial direction, spectral proper orthogonal decomposition (SPOD) is applied in the near-pressure field to remove the contribution of acoustic fluctuations that contaminate the signal. The first SPOD eigenvector, which has the highest energy content, is shown to display the characteristics of instability waves, with a clear trend of growth, saturation and decay. This trend can be modelled with a Gaussian envelope, which is related to the hydrodynamic wavelength, thus being frequency-dependent. The amplitude of the Gaussian at different axial positions, for each frequency, is found to be an appropriate scaling parameter for the installed far-field noise. The scaled spectra from configurations with different plate lengths collapse in the entire frequency range of the installation effects. Therefore, in order to correctly assess the effects of the near-field characteristics on the far-field noise, it is necessary that the coherent part of the flow field is educed beforehand.

The methodologies developed in this work are shown to be valid when the plate trailing edge is positioned in the linear hydrodynamic field of the jet. Therefore, the constraints for the validity of the approach are: no grazing flow on the plate and thus  $h/L > \tan(\delta)$ , where  $\delta$  is the spreading angle of the jet; the trailing edge must not be placed in the jet acoustic field, where there will be no sound amplification due to installation. Based on the results in this paper, a conservative upper bound for the linear hydrodynamic field, in the frequency range of interest for the investigated plate lengths ( $St \approx 0.2$ ), would be  $h/D_j < 2.5$ . Additionally, for very short and very long plates (e.g.  $L/D_j < 3$  or  $L/D_j > 10$ ), a proper Gaussian fitting of the wavepacket in the isolated jet would not be possible.

It is concluded that the characteristics of the jet pressure field have a strong influence on the noise produced by the scattering at the plate trailing edge. The scaling analysis can be used, for example, to save on costs of simulating or testing several geometric configurations. If the flow-field information is available for the isolated case, the data can be used to predict the far-field characteristics of the installation effects. The compactness analysis provides an interesting method for equivalent source localization, which outputs the frequency envelope of the noise amplification for the installed case. Therefore, by making use of the near-field properties of the jet, the surface can be dimensioned to restrict the frequencies where the amplification occurs or, for example, shift the far-field peak to frequencies where the scattering is no longer the dominant source, resulting in significant noise reductions.

## Acknowledgements

This work is part of the IPER-MAN project (Innovative PERmeable Materials for Airfoil Noise Reduction), project no. 15452. The authors would like to thank: C. Brown, from NASA Glenn, for sharing the experimental data from the jet-surface interaction tests; and Dr O. Schmidt and Professor Dr T. Colonius, from Caltech, for sharing the SPOD code used in this work. The authors would like to acknowledge Dr W. van der Velden, from Dassault Systemes, for providing the set-up of the isolated nozzle. The authors would also like to thank Dr M. Snellen and Professor S. van der Zwaag, from Delft University of Technology, for collaboration in the project.

## Declaration of interests

The authors report no conflict of interest.

## Appendix A

A brief description of the procedure adopted for the decomposition of the near pressure field of the jet follows. For a more detailed explanation of the method, the reader is referred to Schmidt *et al.* (2018) and Towne *et al.* (2018). The SPOD is based on the decomposition of the cross-spectral density tensor, leading to energy-ranked modes, in the form of coherent structures, that each oscillate at a single frequency. These modes are orthogonal to each other at any frequency and, as a set, optimally represent the space–time flow statistics (Schmidt *et al.* 2018).

For the decomposition of a given flow-field property  $\mathbf{q}(\mathbf{x}, t)$  into orthogonal modes in the frequency domain, the cross-spectral density tensor is necessary. The tensor can be obtained, for example, using the method of snapshots, which is commonly used for space-only POD (Sirovich 1987). Welch's method (Welch 1967) is applied to average the spectra over multiple realizations of the flow in order to ensure convergence for analyses with a large number of snapshots. The data are split into blocks, for which the Fourier coefficients are computed, allowing the cross-spectral density tensor to be determined for each frequency (Towne *et al.* 2018). In order to obtain the SPOD modes, the following spectral eigenvalue problem must be solved:

$$\int_{\Omega} \mathbf{S}(\mathbf{x}, \mathbf{x}', f') \mathbf{W}(\mathbf{x}') \psi(\mathbf{x}', f') d\mathbf{x}' = \lambda(f') \psi(\mathbf{x}, f'), \quad (\text{A } 1)$$

where  $\mathbf{S}$  is the cross-spectral density tensor, and the weight  $\mathbf{W}$  is a positive-definite Hermitian tensor. The eigenvectors  $\psi$ , with their respective eigenvalue  $\lambda$ , are computed for a given frequency  $f'$  (Towne *et al.* 2018). Thus, the Fourier modes of the flow field  $\hat{\mathbf{q}}(\mathbf{x}, f)$  can be expanded as

$$\hat{\mathbf{q}}(\mathbf{x}, f) = \sum_{j=1}^{\infty} a_j(f) \psi_j(\mathbf{x}, f), \quad (\text{A } 2)$$

where  $a_j(f) = \langle \hat{\mathbf{q}}(\mathbf{x}, f), \psi_j(\mathbf{x}, f) \rangle_x$ . According to Towne *et al.* (2018), for the space-only POD, a stochastic flow ensemble is obtained from snapshots of the flow field at different time instants, representing a realization of the stochastic process. The time evolution of the flow has no effect on those modes, and a temporal correlation of the data is not possible. Therefore, the space-only POD modes are composed of structures at many frequencies, which do not necessarily evolve coherently in time. In the spectral POD, on the other hand, the stochastic ensemble is based on realizations of the time-dependent flow. Each SPOD mode is perfectly correlated with itself at all times, and thus they provide spatiotemporal coherent structures, which is the focus of the analysis intended in this work.

## REFERENCES

- ARNDT, R. E. A., LONG, D. F. & GLAUSER, M. N. 1997 The proper orthogonal decomposition of pressure fluctuations surrounding a turbulent jet. *J. Fluid Mech.* **340**, 1–33.

- BELYAEV, I., FARANOSOV, G., OSTRIKOV, N. & PARANIN, G. 2015 A parametric experimental study of jet-flap interaction noise for a realistic small-scale swept wing model. In *21st AIAA/CEAS Aeroacoustics Conference, AIAA Paper* 2015-2690.
- BREAKEY, D. E. S., JORDAN, P., CAVALIERI, A. V. G., LÉON, O., ZHANG, M., LEHNASCH, G., COLONIUS, T. & RODRIGUEZ, D. 2013 Near-field wavepackets and the far-field sound of a subsonic jet. In *19th AIAA/CEAS Aeroacoustics Conference, AIAA Paper* 2013-2083.
- BRÈS, G., NICHOLS, J. W., LELE, S. & HAM, F. E. 2012 Towards best practices for jet noise predictions with unstructured large eddy simulations. In *42nd AIAA Fluid Dynamics Conference and Exhibit, AIAA Paper* 2012-2965.
- BRÈS, G., PÉROT, F. & FREED, D. 2009 Properties of the lattice Boltzmann method for acoustics. In *15th AIAA/CEAS Aeroacoustics Conference, AIAA Paper* 2009-3395.
- BRÈS, G., PÉROT, F. & FREED, D. 2010 A Ffowcs Williams–Hawkings solver for lattice-Boltzmann based computational aeroacoustics. In *16th AIAA/CEAS Aeroacoustics Conference, AIAA Paper* 2010-3711.
- BRIDGES, J. & WERNET, M. 2010 Establishing consensus turbulence statistics for hot subsonic jets. In *16th AIAA/CEAS Aeroacoustics Conference, AIAA Paper* 2010-3751.
- BROWN, C. 2012 Jet-surface interaction test: far-field noise results. In *Proceedings of the ASME Turbo Expo 2012: Power for Land, Sea and Air, Paper* GT2012-69639, pp. 1–13.
- BROWN, C. & BRIDGES, J. 2006 Small hot jet acoustic rig validation. *Tech. Rep. NASA/TM-2001-214234*, Cleveland, OH, USA.
- BROWN, W. H. & AHUJA, K. K. 1984 Jet and wing/flap interaction noise. In *AIAA/NASA 9th Aeroacoustics Conference, AIAA Paper* 1984-2362.
- CASALINO, D. 2003 An advanced time approach for acoustic analogy predictions. *J. Sound Vib.* **261** (4), 583–612.
- CASALINO, D., AVALONE, F., GONZALEZ-MARTINO, I. & RAGNI, D. 2019 Aeroacoustic study of a wavy stator leading edge in a realistic fan/OGV stage. *J. Sound Vib.* **442**, 138–154.
- CASALINO, D. & HAZIR, A. 2014 Lattice Boltzmann based aeroacoustic simulation of turbofan noise installation effects. In *23rd International Congress on Sound and Vibration*, pp. 1–8.
- CASALINO, D., HAZIR, A. & MANN, A. 2017 turbofan broadband noise prediction using the lattice Boltzmann method. *AIAA J.* **56** (2), 609–628.
- CAVALIERI, A. V. G., JORDAN, P., COLONIUS, T. & GERVAIS, Y. 2012 Axisymmetric superdirectivity in subsonic jets. *J. Fluid Mech.* **704**, 388–420.
- CAVALIERI, A. V. G., JORDAN, P., WOLF, W. R. & GERVAIS, Y. 2014 Scattering of wavepackets by a flat plate in the vicinity of a turbulent jet. *J. Sound Vib.* **333** (24), 6516–6531.
- CHEN, H., CHEN, S. & MATTHAEUS, W. H. 1992 Recovery of the Navier–Stokes equations using a lattice-gas Boltzmann method. *Phys. Rev. A* **45** (8), 5339–5342.
- CHEN, H., GOPALAKRISHNAN, P. & ZHANG, R. 2014 Recovery of Galilean invariance in thermal lattice Boltzmann models for arbitrary Prandtl number. *Intl J. Mod. Phys. C* **25** (10), 1–14.
- CHEN, H., ORSZAG, S. A., STAROSELSKY, I. & SUCCI, S. 2004 Expanded analogy between Boltzmann kinetic theory of fluids and turbulence. *J. Fluid Mech.* **519**, 301–314.
- COLONIUS, T., LELE, S. K. & MOIN, P. 1997 Sound generation in a mixing layer. *J. Fluid Mech.* **330**, 375–409.
- CRIGHTON, D. G. & HUERRE, P. 1990 Shear-layer pressure fluctuations and superdirective acoustic sources. *J. Fluid Mech.* **220**, 355–368.
- CRIGHTON, D. G. & LEPPINGTON, F. G. 1970 Scattering of aerodynamic noise by a semi-infinite compliant plate. *J. Fluid Mech.* **43**, 721–736.
- CROW, S. C. 1972 Acoustic gain of a turbulent jet. In *Phys. Soc. Meeting, Paper IE*, vol. 6.
- FARASSAT, F. & SUCCI, G. P. 1980 A review of propeller discrete frequency noise prediction technology with emphasis on two current methods for time domain calculations. *J. Sound Vib.* **71** (3), 399–419.
- FFOWCS-WILLIAMS, J. E. & HALL, L. H. 1970 Aerodynamic sound generation by turbulent flow in the vicinity of a scattering half plane. *J. Fluid Mech.* **40** (4), 657–670.
- FFOWCS-WILLIAMS, J. E. & HAWKINGS, D. L. 1969 Sound generation by turbulence and surfaces in arbitrary motion. *Phil. Trans. R. Soc. Lond. A* **264** (1151), 321–342.



- GONZALEZ-MARTINO, I. & CASALINO, D. 2018 Fan tonal and broadband noise simulations at transonic operating conditions using lattice-Boltzmann methods. In *2018 AIAA/CEAS Aeroacoustics Conference, AIAA Paper* 2018-3919.
- HEAD, R. W. & FISHER, M. J. 1976 Jet/surface interaction noise: – analysis of farfield low frequency augmentations of jet noise due to the presence of a solid shield. In *3rd AIAA Aeroacoustics Conference, AIAA Paper* 1976-502.
- HUFF, D. L. 2007 Noise reduction technologies for turbofan engines. *NASA/TM-2007-214495*. pp. 1–17.
- JORDAN, P. & COLONIUS, T. 2013 Wave packets and turbulent jet noise. *Annu. Rev. Fluid Mech.* **45**, 173–195.
- LAUFER, J. & YEN, T. 1983 Noise generation by a low-Mach-number jet. *J. Fluid Mech.* **134**, 1–31.
- LAUNDER, B. E. & SPALDING, D. B. 1974 The numerical computation of turbulent flows. *Comput. Meth. Appl. Mech. Engng* **3** (2), 269–289.
- LAWRENCE, J. L. T., AZARPEYVAND, M. & SELF, R. H. 2011 Interaction between a flat plate and a circular subsonic jet. In *17th AIAA/CEAS Aeroacoustics Conference, AIAA Paper* 2011-2745.
- LIGHTHILL, M. J. 1952 On sound generated aerodynamically. I. General theory. *Proc. R. Soc. Lond. A* **211** (1107), 564–587.
- LYU, B., DOWLING, A. P. & NAQAVI, I. 2017 Prediction of installed jet noise. *J. Fluid Mech.* **811**, 234–268.
- MENGLE, V. G., BRUSNIAK, L., ELKOBY, R. & THOMAS, R. H. 2006 Reducing propulsion airframe aeroacoustic interactions with uniquely tailored chevrons: 3. Jet–flap interaction. In *12th AIAA/CEAS Aeroacoustics Conference, AIAA Paper* 2006-2435.
- PAPAMOSCHOU, D. 2010 Prediction of jet noise shielding. In *48th AIAA Aerospace Sciences Meeting Including the New Horizons Forum and Aerospace Exposition, AIAA Paper* 2010-653.
- PIANTANIDA, S., JAUNET, V., HUBER, J., WOLF, W., JORDAN, P. & CAVALIERI, A. V. G. 2016 Scattering of turbulent-jet wavepackets by a swept trailing edge. *J. Acoust. Soc. Am.* **140** (6), 4350–4359.
- PODBOY, G. G. 2013 Jet–surface interaction test: phased array noise source localization results. *NASA/TM-2013-218085*.
- ROGER, M., MOREAU, S. & KUCUKCOSKUN, K. 2016 On sound scattering by rigid edges and wedges in a flow, with applications to high-lift device aeroacoustics. *J. Sound Vib.* **362**, 252–275.
- SCHMIDT, O. T., TOWNE, A., RIGAS, G., COLONIUS, T. & BRÈS, G. A. 2018 Spectral analysis of jet turbulence. *J. Fluid Mech.* **855**, 953–982.
- DA SILVA, F. D., DESCHAMPS, C. J., DA SILVA, A. R. & SIMÕES, L. G. C. 2015 Assessment of jet–plate interaction noise using the lattice Boltzmann method. In *21st AIAA/CEAS Aeroacoustics Conference, AIAA Paper* 2015-2207.
- SIROVICH, L. 1987 Turbulence and the dynamics of coherent structures. Part I. Coherent structures. *Q. Appl. Maths* **XLV**, 561–571.
- SUCCI, S. 2001 *The Lattice Boltzmann Equation for Fluid Dynamics and Beyond*. Oxford University Press.
- SUZUKI, T. & COLONIUS, T. 2006 Instability waves in a subsonic round jet detected using a near-field phased microphone array. *J. Fluid Mech.* **565**, 197–226.
- TINNEY, C. E. & JORDAN, P. 2008 The near pressure field of co-axial subsonic jets. *J. Fluid Mech.* **611**, 175–204.
- TOWNE, A., SCHMIDT, O. T. & COLONIUS, T. 2018 Spectral proper orthogonal decomposition and its relationship to dynamic mode decomposition and resolvent analysis. *J. Fluid Mech.* **847**, 821–867.
- UNNIKRISHNAN, S., CAVALIERI, A. V. G. & GAITONDE, D. V. 2019 Acoustically informed statistics for wave-packet models. *AIAA J.* **57**, 2421–2434.
- VAN DER VELDEN, W. C. P., CASALINO, D., GOPALAKRISHNAN, P., JAMMALAMADAKA, A., LI, Y., ZHANG, R. & CHEN, H. 2018 Jet noise prediction: validation and physical insight. In *24th AIAA/CEAS Aeroacoustics Conference, AIAA Paper* 2018-3617.

- WELCH, P. 1967 The use of fast Fourier transform for the estimation of power spectra: a method based on time averaging over short, modified periodograms. *IEEE Trans. Audio Electroacoust.* **15** (2), 70–73.
- YAKHOT, V. & ORSZAG, S. A. 1986 Renormalization group analysis of turbulence. I. Basic theory. *J. Sci. Comput.* **1** (1), 3–51.
- YAKHOT, V., ORSZAG, S. A., THANGAM, S., GATSKI, T. B. & SPEZIALE, C. G. 1992 Development of turbulence models for shear flows by a double expansion technique. *Phys. Fluids A* **4** (7), 1510–1520.